MULTI-LAYER RELAXATION MODELS FOR HEATING IN CORONAL LOOPS

A dissertation submitted to the University of Manchester
for the degree of Master of Science
in the Faculty of Science and Engineering
department of Physics and Astronomy

September 2019

Shahbaz Chaudhry

School of Natural Sciences

Contents

List of Tables

List of Figures

Abstract

Solar coronal heating is a long standing problem in astrophysics. One possible explanation is that discrete heating events known as nanoflares heat the solar corona to millions of degrees. However, due to their size, nanoflares are difficult to detect, hence theoretical calculations are required to determine the viability of coronal heating by nanoflares. Relaxation theory (Taylor [1974], Taylor [1986]) provides a formalism wherein the minimum energy principle (Woltjer [1960]) can be used to calculate energy release from nanoflares.

Understanding relaxation theory requires knowledge of magnetohydrodynamics (MHD), including a quantity known as magnetic helicity. Cylindrical relaxation models have been used to calculate energy release from discrete heating events or nanoflares. Building upon work previously done on cylindrical relaxation models in Browning [2003] (two layers) and Bareford et al. [2011] (three layers), a multi-layer cylindrical model is constructed, valid for an arbitrary number of layers. Cylindrical models allow for a simplified geometry which results in analytic solutions. The model is constructed as embedded concentric cylinders each with a magnetic field which is continuous across the layer boundary.

The code is tested and then used to calculate quantities such as helicity transfer and energy. These values are used to verify a process known as hyperdiffusion (Van Ballegooijen and Cranmer [2008], Bhattacharjee and Hameiri [1986], Boozer [1986]), which offers insight into the process of relaxation. Results from the multi-layer model lend some support to hyperdiffusion being responsible for relaxation in cylindrical flux tubes. More research is needed however to determine if this is the case in the corona and what observable signatures will be present as a result. The model also provides a useful tool for calculating analytical models of force-free magnetic fields, which may be used for a variety of purposes.

Declaration

No portion of the work referred to in this dissertation has been submitted in support of an application for another degree or qualification of this or any other university or other institute of learning.

Copyright

i. The author of this thesis (including any appendices and/or schedules to this thesis) owns certain copyright or related rights in it (the "Copyright") and s/he has given The University of Manchester certain rights to use such Copyright, including for administrative purposes.

ii. Copies of this thesis, either in full or in extracts and whether in hard or electronic copy, may be made **only** in accordance with the Copyright, Designs and Patents Act 1988 (as amended) and regulations issued under it or, where appropriate, in accordance with licensing agreements which the University has from time to time. This page must form part of any such copies made.

iii. The ownership of certain Copyright, patents, designs, trade marks and other intellectual property (the "Intellectual Property") and any reproductions of copyright works in the thesis, for example graphs and tables ("Reproductions"), which may be described in this thesis, may not be owned by the author and may be owned by third parties. Such Intellectual Property and Reproductions cannot and must not be made available for use without the prior written permission of the owner(s) of the relevant Intellectual Property and/or Reproductions.

iv. Further information on the conditions under which disclosure, publication and commercialisation of this thesis, the Copyright and any Intellectual Property and/or Reproductions described in it may take place is available in the University IP Policy (see http://documents.manchester.ac.uk/DocuInfo.aspx?DocID=487), in any relevant Thesis

restriction declarations deposited in the University Library, The University Library's regulations (see http://www.manchester.ac.uk/library/aboutus/regulations) and in The University's policy on presentation of Theses

Acknowledgements

I would like to thank my supervisor Philippa for her guidance through-out the project and my parents for their support.

Chapter 1

Introduction

A current problem in astrophysics is trying to understand the mechanism by which the temperature of the corona counter-intuitively reaches three order of magnitude larger in temperature than the solar surface.

As the Sun is composed of plasma, to understand the coronal heating problem plasma dynamics must be understood. Magnetohydrodynamics (MHD) is one way to describe plasma motion of all species in a charged fluid. The other being kinetic theory which separately treats each species separately with a distribution function, due to the large length scales involved in the corona we will utilise MHD instead. One application of plasma dynamics includes space weather, as it allows for the protection of satellites and power grids. In 1989, after an extreme space weather event, the power for 6 million people was cut off for 9 hours in Quebec, Canada (Allen et al. [1989]). Another application lies in nuclear fusion where MHD can be used to simulate plasma behaviour within a tokamak (a device which uses strong magnetic field to confine hot plasmas) to more efficiently calibrate fusion systems for energy output. The relationship between nuclear fusion and astrophysical plasma physics can be seen in Taylor [1974] where relaxation theory was first used to calculate the energy release from within a tokamak.

The corona has been observed as being permeated by filament-like structures known as magnetic flux tubes. The structure of these flux tubes is cylindrical and such cylindrical polar co-ordinates will be heavily further on in this thesis. Most theories of coronal heating rely on processes involving these flux tubes. The principal mechanism by which magnetic energy can be

converted into thermal energy is through Ohmic dissipation resulting in magnetic reconnection. The power of relaxation theory lies in the fact that only the initial energy state of the system is needed. Therefore using relaxation theory the complex intermediary non-linear dynamics can be bypassed and the final energy state and hence energy release can be calculated. The mathematical derivation was first performed in Woltjer [1960] and then expanded by Taylor (Taylor [1974], Taylor [1986]) for use on real plasma. One draw back of relaxation theory is time dependant information is not obtained. Therefore, resistive MHD simulations or reconnection models are required to obtain heating.

In 1964, Gold coined the term for discrete heating events as 'nano-flares' (Gold [1964]). Later Parker (Parker [1983]) refined the concept suggesting that many small rapid releases of magnetic energy can sustain coronal temperatures. Nano-flares arise from photospheric footpoint motion twisting magnetic flux tubes of the order 1500 G and approximately 10 - 100 Mm in length (Klimchuk [2015]). Upon reaching a critical threshold of twist an instability is formed which leads to a relaxation of the flux tube and the appearance of a localised transient brightening. In the process of relaxation magnetic energy is converted into thermal energy.

In this thesis, I create a code to generate a multi-layer cylindrical relaxation model. The model can create an arbitrary number of concentric cylinders each with an initial configurable magnetic field, continuous across the boundary. Concentric cylindrical fields were first proposed by Melrose et al. [1994] to model flux ropes. The benefit of using a multi-layer cylindrical model is that quantities such as helicity are analytic. The multi-layer relaxation model will be compared to previous work done by Browning [2003] and Bareford et al. [2010] before moving forward.

The multi-layer code will be then used to verify whether a process known as hyperdiffusion (Van Ballegooijen and Cranmer [2008], Bhattacharjee and Hameiri [1986], Boozer [1986]) takes place in the model. In the theory of hyperdiffusion a quantity known as helicity is conserved in a turbulent magnetic field and is thought to be the mechanism behind relaxation. To confirm whether hyperdiffusion takes place relationships for energy release and helicity transfer will be sought. Finally, the difference between values of helicity and energy for different field profiles will be compared.

1.1 The Solar Atmosphere

In order to move forward with coronal heating we must first understand the structure and function of the constituent parts of the solar atmosphere. All parts of the solar atmosphere are affected by strong magnetic fields giving rise to structures which we will later see play a large role in coronal heating (Figure 1.1). The solar atmosphere is made up of three parts each with distinct temperate and pressure gradients (Figure 1.2).

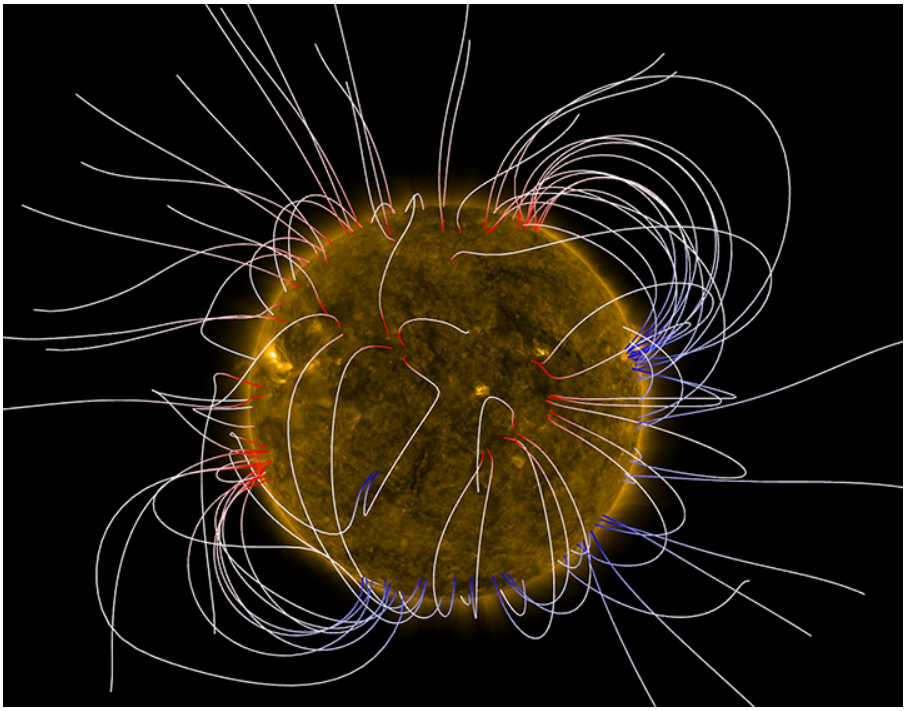

Figure 1.1: Magnetic field lines superimposed on an image of the corona, showing the extent of magnetic activity on the solar atmosphere, red and blue field line ends refer to opposing polarities (NASA/SDO [Dec, 2016]).

The lowest part of the solar atmosphere is the photosphere which is approximately 1000 km deep and extends down to the solar surface and where photons of light are emitted. Upon closer inspection the photosphere is not uniformly bright and is superimposed with structures known as granules and sunspots (Figure 1.3). Granules arise due to convective motion beneath the photosphere and have an average lifetime of 5-10 minutes, bright sports correspond to hot rising less dense plasma and the dark spots represent cool falling material. Unlike granules sunspots are larger and are regions of high magnetic flux. As a result, they have an associated magnetic pressure, reducing the thermal pressure within and causing the temperature inside to be lower, as such they appear darker. Sun spots often come in pairs and have opposing polarity

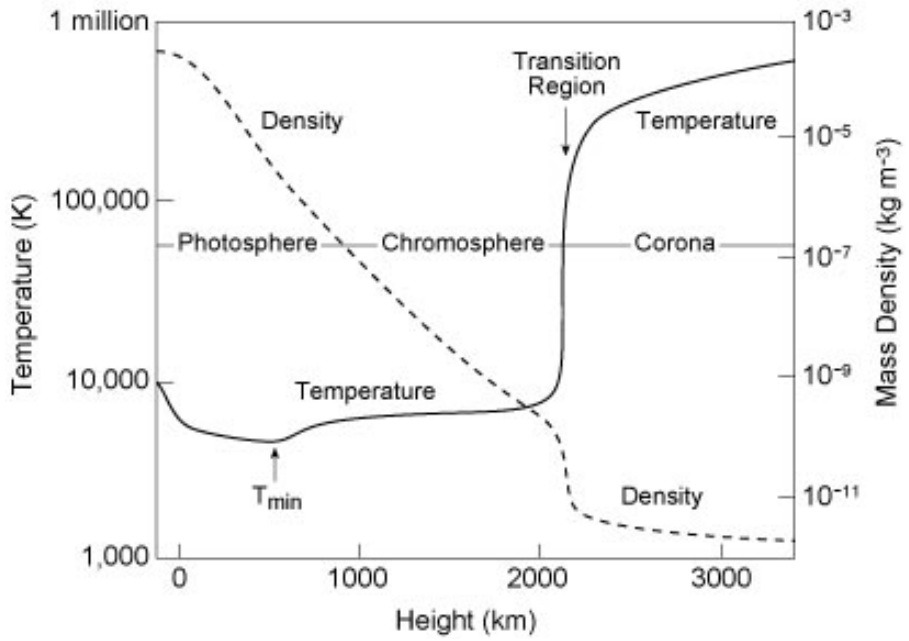

Figure 1.2: A graph of temperature and density of varying regions of the solar atmosphere magnetic field (Lang, KR [2019]).

on different hemispheres of the sun. Intersecting these sunspot pairs are structures known as magnetic flux tubes, analogous to field lines on a bar magnet. Typical values for the magnetic field around sunspots is 1 kG compared to the ambient field of 100 G around the photosphere. The number of sunspots varies over an 11 year cycle, although there is long term variation on a roughly 205 year period known as the de Vries cycle (Priest [2012]).

Compared to the photosphere, the chromosphere is more transparent and is less dense, with a characteristic red Hα emission. At the limb of the chromosphere many small plasma jets can be seen, known as spicules (Figure 1.4) which are ejected at granule boundaries with an average lifetime of 3-10 minutes (Priest [2012]).

The corona extends past the chromosphere and has no definitive end, reaching a maximum temperature of around 10^6K (Figure 1.1), and decreasing further out. The corona is clearly visible during a solar eclipse in the visible spectrum. Otherwise the corona can be seen directly in the soft X-ray part of the spectrum via space telescopes such as the Solar Dynamics Observatory (SDO). From images taken of the corona during a solar eclipse filament like structures can be seen known as solar streamers surrounding regions of high magnetic flux such as sunspots and are more frequent during the peak of the 11 year cycle (Figure 1.5). During times of greater solar activity greater amounts of charged particles are ejected from regions

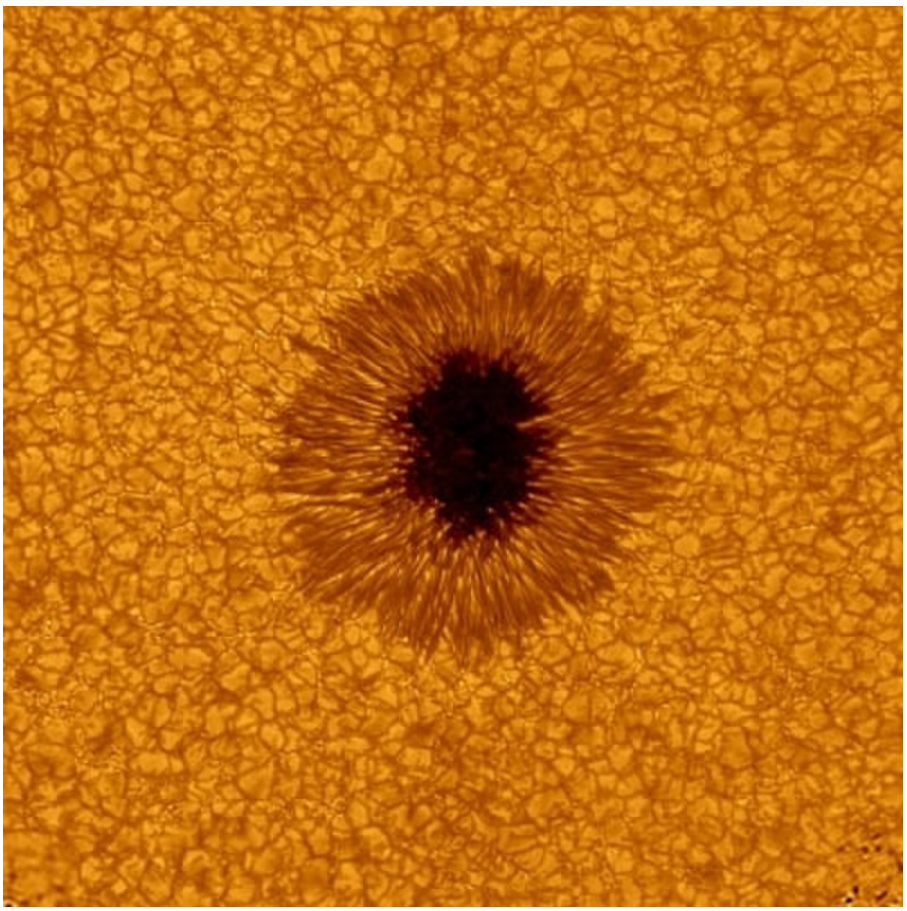

Figure 1.3: A sunspot on the photosphere surrounded by granules arising due to thermal fluctuations. (Observatory [Aug, 2010]).

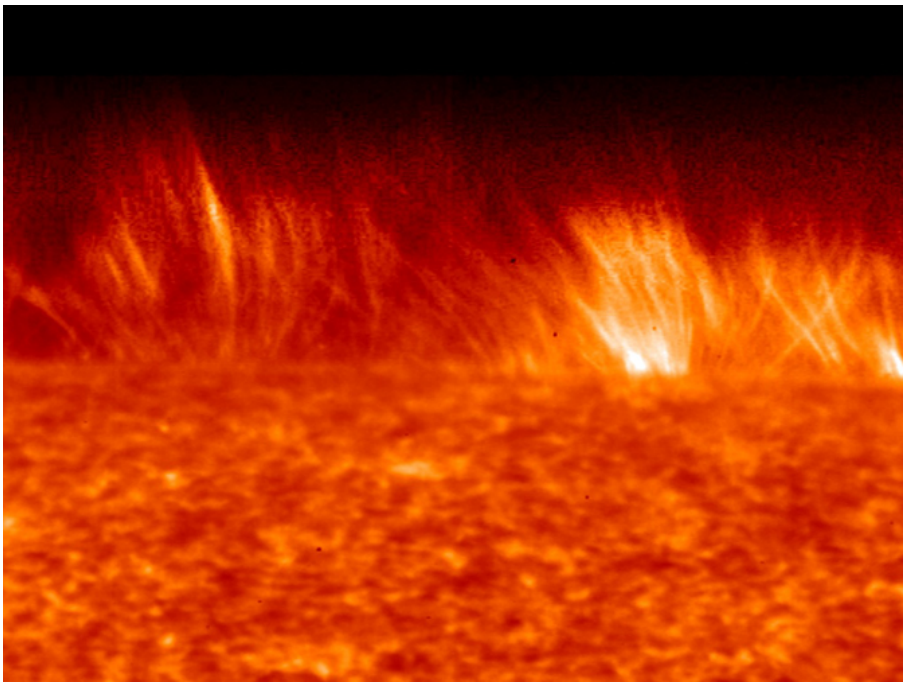

Figure 1.4: An image taken at the limb of the chromosphere showing a 'forest' of solar spicules JAXA/Hinode [(June, 2013]

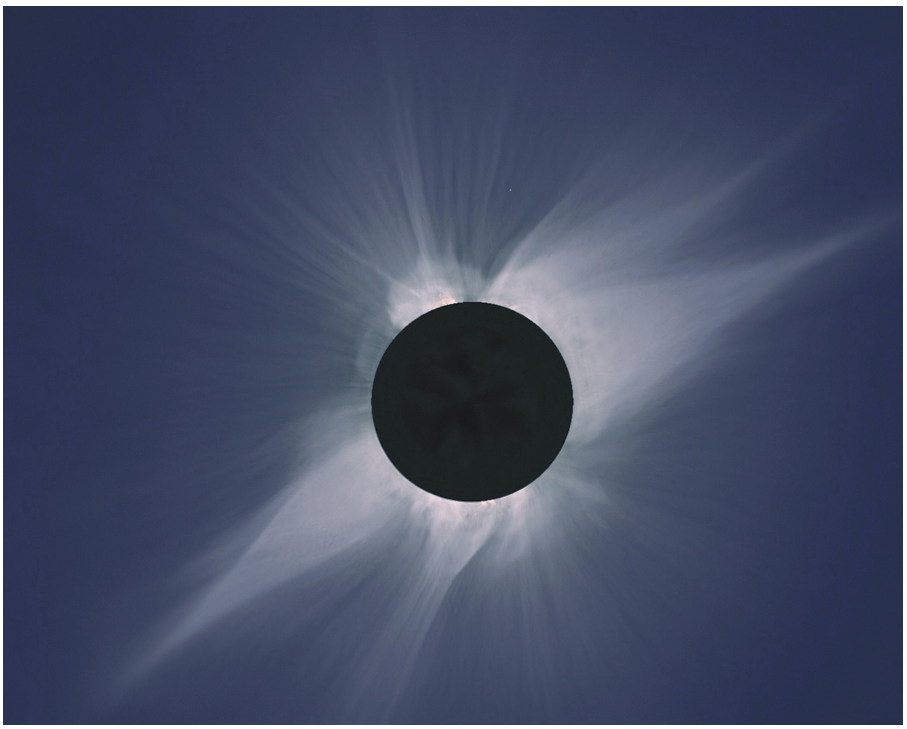

Figure 1.5: A solar eclipse with the corona and solar streamers visible (Steve and Dennis [(July 11, 1991]).

surrounding sunspots and larger coronal holes where magnetic field lines appear open and give rise to the solar wind (Golub and Pasachoff [2010]). During solar maximum (the peak of the 11 year cycle) more particles are ejected from open regions and the strength of the solar wind increases such that extreme space weather events become more likely. During solar maximum large magnetic features such as prominences become visible (Figure 1.6). Moving forward the

Figure 1.6: A close up of a solar flare (top left), the solar prominence is stretched outwards until it finally breaks and becomes a CME (Sept. 3, 2012 NASA/SDO [Aug, 2012]).

same mechanisms at play for Coronal Mass Ejections (CMEs) and Solar flares (Figure 1.6) will

be important to understand discrete heating by nanoflares.

Solar flares often but not always lead to CMEs and can be defined as localised transient brightening. The energy released in a flare typically ranges from 10^{22}J in a sub flare to 6×10^{25}J and above (see Emslie et al. [2005] for detailed flare and CME energy breakdown). CMEs can be defined as large scale expanding plasma masses moving away from the sun. The charged particles from CMEs can damage spacecraft and earth based electronic systems and on average the kinetic energy of a CME is similar to that of a flare. Approximately 2 CMEs occur per day at solar minimum and 8 per day at solar maximum (Robbrecht et al. [2009]). While flares reach the earth in about 8 minutes, CMEs can take anywhere between 5 days to 80 minutes to reach the earth.

The main source of energy for flares or CMEs are necessarily the magnetic fields given that no other major sources of free energy are available to explain observations of energy. One way to increase the available free energy is through a process known as magnetic reconnection. Solar activity is divided into two regimes: the active sun and the quiet sun. The active sun refers to parts of the Sun responsible for transient behaviour such as flares and CMEs and is superimposed upon the quiet sun. The quiet sun is the near constant background, which will be of interest in coronal heating. In section 2.4, we will see there exists a standard flare and CME model which will be looked into in more detail (see section on magnetic reconnection). Understanding flares and CMEs from active sun phenomena will help to understand nanoflare heating in the quiet sun as many of the same processes are involved.

1.2 The Coronal Heating Problem

The coronal heating problem requires a mechanism by which the energy losses due to conduction and radiation can be balanced to maintain sufficiently high temperature. Upon observation of the corona it can be seen to be highly magnetic. It is this magnetic structure which is thought to play a key part in coronal heating. Globally the corona is highly conducting and hence Ohmic dissipation rates are low (see induction equation 2.9), therefore heating must take place on smaller length scales than MHD length scales.

A definitive theory of coronal heating therefore requires the coupling of large scale effects (photospheric driving) to small scale ones (where energy dissipation can take place), while taking into account the different densities and structures in the solar atmosphere.

The difficulty lies in determining the details, i.e the responsible dissipation mechanism(s) which occur on small length scales. All current mechanisms for coronal heating require kinetic energy being transferred from beneath the photosphere into magnetic energy above which is then dissipated. Beyond that theories can be classed as either AC or DC heating, depending on the timescale of photospheric driving and Alfvén wave time. Where Alfvén waves are MHD waves arising from ions oscillating in response to the restoring force of magnetic tension (Figure 1.7 and section on MHD) along field lines.

AC heating

AC heating requires Alfvén wave time scales across coronal fields to be large compared to foot-point motion time-scales causing the fields to oscillate and results in wave-like behaviour.

For AC heating, two key hurdles are the efficiency of transmission and dissipation. Turbulent convection is thought to generate Alfvén waves and sound waves which propagate upwards. Only a small number of waves are able to pass through to the corona, due to the large pressure and temperature gradients. Slow sound waves produce shocks and are damped, while fast sound waves are reflected. Alfvén waves are most able to penetrate the corona as they are transverse thus do not form shocks when passing though the solar atmosphere.

Alfvén waves can still be reflected in chromosphere and transition region as they speed up

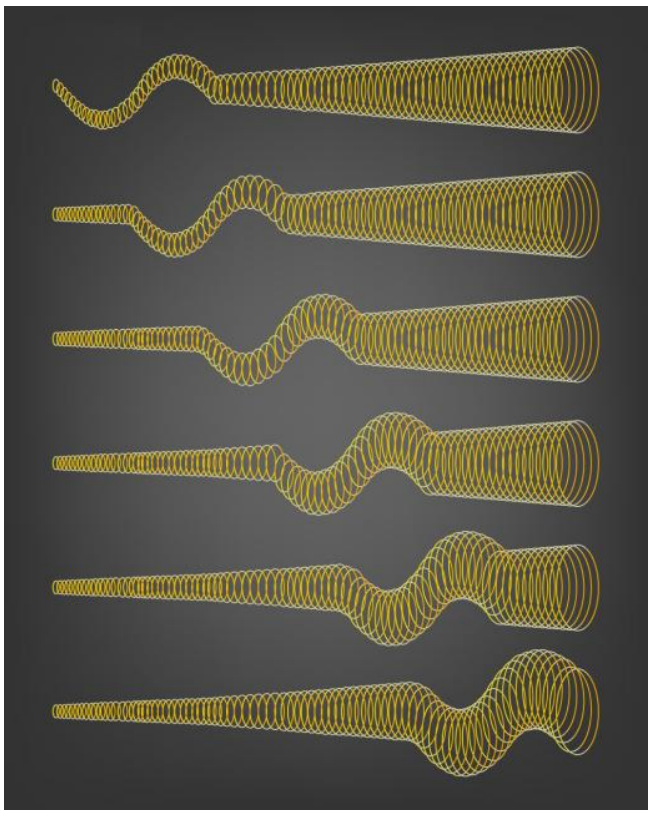

Figure 1.7: A helical magnetic field (yellow coil) suspended in plasma with an Alfvén wave travelling along the magnetic field (NASA/JPL-Caltech [(Sept, 2015])

further away from the photosphere. Substantial transmission is possible only within narrow frequency bands centred on discrete values where the coronal loops resonate (Hollweg [1981]). However, transmission can be bypassed by waves generated in the corona which have been measured (Erdélyi et al. [2004]). More investigation is required to determine whether waves generated in the corona have sufficient energy and if so how these waves dissipate energy to heat the surrounding plasma. Better measurements of coronal wave flux and dissipation mechanisms is key for the viability of AC heating.

DC heating

With DC heating the opposite is true, Alfvén wave speed is small relative to photospheric driving motion, hence minimising wave-like behaviour and resulting in the braiding or twisting of field lines in flux ropes of around kG magnitude (Figure 1.8).

An important constraint for DC heating arises from the Pointing flux of energy which can be

given as

$$F = \frac{1}{\mu} B_v B_h v_h \tag{1.1}$$

Where B_v is the vertical component of the field, B_h is the horizontal component and v_h is the horizontal photospheric footpoint velocity. Taking typical low corona values for the vertical magnetic field taken using longitudinal magnetograms we find $B_v \approx 100G$ in active regions (Schrijver and Harvey [1994]) and roughly 10 times less in the quiet sun. Turbulent convection at the photosphere displaces magnetic flux tubes and move about the surface with $v_h \approx 1kms^{-1}$ et al.. We can assume that flux tubes move with similar velocity in the low corona. In order to balance the energy loses of $10^4\ Wm^{-2}$ around active regions B_h must be around 10% or more of B_v (Parker [1988]). Coronal flux tubes can become tangled from random motion arising from turbulent convection as long as the displacement from v_h is larger than the separation of neighbouring flux tubes. As B_h builds up the magnetic fields becomes more tilted and stresses build until instabilities arise and dissipate the energy of the braided flux tube (see section 2.4). This simple constraint on B_h is important because if magnetic stresses were not allowed to build up and activated earlier or later then the corona would be either colder or hotter than observed.

It is clear that DC heating is viable to sustain large coronal temperatures. However, what is not clear is how magnetic energy is converted into thermal energy as global Ohmic heating is too inefficient. A more viable mechanism as we will later see is magnetic reconnection (section 2.4).

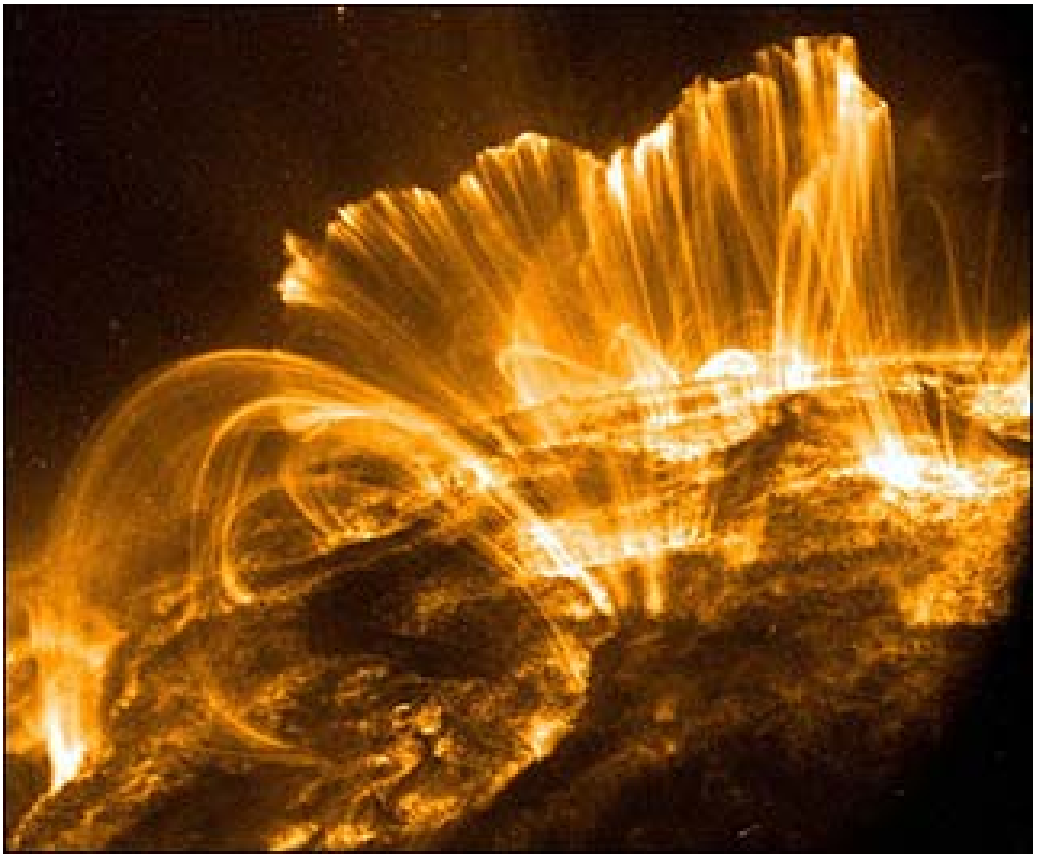

Figure 1.8: A close up of magnetic structures in the corona where flux tubes appear braided (TRACE [(Nov, 2000])

Chapter 2

Magnetohydrodynamics

In order to model activity in the solar corona, we will use magnetohydrodynamics (MHD), which is a widely-used tool. Here we only introduce MHD and parts required to understand the text, for more details see Priest [2012], Schnack [2009] and Cowling [1976]. Using a combination of fluid dynamics (Naiver-Stokes) and electromagnetism (Maxwells equations) the governing MHD equations can be derived (Priest [2012]). In the theory of MHD the following assumptions are made; that parameters defining the fluid such as velocity, density and pressure are averaged over infinitesimal volumes Schnack [2009]. Even though a plasma is made up of ions, it will be can be assumed to be a quasi neutral over the typical length scale of the system. Plasma flow is assumed to be sub-relativistic where $v^2/c^2 << 1$ where v is the fluid velocity, such that only low frequency behaviour is taken into account. The mean free path assumed to be smaller than the plasma length scale such that the plasma is said to be collisional. However MHD can even be used to accurately model collisionless plasma such as in the outer corona (solar wind). One reason is that the conservation of energy, mass and momentum are contained within the MHD equations and therefore must apply to both collisional and collisionless plasma (Priest [2012]).

2.1 The MHD equations

First mass continuity is considered

$$\frac{\partial \rho}{\partial t} + \nabla \cdot \rho \mathbf{v} = 0 \tag{2.1}$$

in the frame where the volume element is fixed in space also known as the Eulerian frame Schnack [2009], where ρ is mass density and $\mathbf{v}$ is the fluid velocity vector.

Secondly, The modified Navier-Stokes equation for plasma is obtained by applying Newton's second law to forces acting on the fluid giving

$$\rho\left[\frac{\partial \mathbf{v}}{\partial t} + (\mathbf{v} \cdot \nabla)\mathbf{v}\right] = \mathbf{j} \times \mathbf{B} - \nabla p + \rho \mathbf{g} + \mathbf{F}_{visc} \tag{2.2}$$

The left hand side (LHS) is (equal to $\rho\frac{d\mathbf{v}}{dt}$ in the co-moving frame known as the Lagrangian frame (giving rise to the convective derivative on the LHS) Schnack [2009]). The terms on the right hand side represent the sum of forces acting on the fluid per unit volume, including the Lorentz force, the pressure gradient, gravity and viscous forces, respectively.

As briefly mentioned, a plasma can be approximated as an ideal gas.

$$\rho e = \frac{p}{\Gamma - 1} \tag{2.3}$$

where e is the internal energy per unit mass, p is the pressure and ρ is the density and Γ is the adiabatic index (for a plasma Γ=5/3). From (2.3) it can be seen that the energy is dependent on pressure. Next using the conservation of energy (in the form of the first law of thermodynamics) and the ideal gas law, the following equation for pressure can be obtained (Schnack [2009]),

$$\frac{\partial p}{\partial t} + \mathbf{v} \cdot \nabla p = -\Gamma p \nabla \cdot \mathbf{v} + (\Gamma - 1)[-\nabla \cdot \mathbf{Q} + R_v] \tag{2.4}$$

where the first term on the RHS of (2.4) can be seen as the reversible work and the second term irreversible heating. The volumetric heating rate is R_v and $\mathbf{Q}$ is the heat flux through the surface. The continuity equation can be used to obtain the adiabatic form of the pressure

equation (2.4) to give

$$\frac{d}{dt}\left(\frac{p}{\rho^{\Gamma}}\right) = 0 \tag{2.5}$$

where the terms on the right of (2.4) are zero if the fluid is assumed to be ideal such that it is incompressible, irrotational and nonviscous (Schnack [2009], Priest [2012]).

Next the electromagnetic contribution to plasma motion is considered. Looking back to the force equation (3.2) Newton's second law has been used and can be shown to be invariant under a Galilean transform. However Maxwell's equations are Lorentz invariant , hence incompatible with the equation of plasma motion. Hence, the limit where $v^2/c^2 << 1$ is taken (Schnack [2009]) which reduces Maxwell's equations to Ampere's law

$$\mu_0 \mathbf{j} = \nabla \times \mathbf{B} \tag{2.6}$$

and

$$\frac{\partial \mathbf{B}}{\partial t} = -\nabla \times \mathbf{E} \tag{2.7}$$

Faraday's law. From these we can deduce $\nabla \cdot \mathbf{B} = 0$ is given by Faraday's law and $\nabla \cdot \mathbf{j} = 0$ by Ampere's law, both are physical constraints. Due to the non relativistic limit MHD excludes electromagnetic radiation.

To find how the magnetic field varies over time Ohm's law for a moving conductor is first considered,

$$\mathbf{j} = \sigma(\mathbf{E} + \mathbf{v} \times \mathbf{B}) \tag{2.8}$$

where the second term inside the brackets takes into account current induced by the Lorentz force and σ is the electrical conductivity. Combining Ohm's law with the non-relativistic form of Maxwell's equations

$$\frac{\partial \mathbf{B}}{\partial t} = \nabla \times (\mathbf{v} \times \mathbf{B}) + \eta \nabla^2 \mathbf{B} \tag{2.9}$$

the magnetic induction equation is obtained, where $\eta = \frac{1}{\mu_0 \sigma}$ and is known as the magnetic diffusivity (Priest [2012]).

Considering the ratios of the magnitudes of the two terms on the right hand side of the induction equation, the magnetic Reynolds number $Re = \frac{Lv}{\eta}$ can be obtained. When $Re << 1$ the plasma

is highly resistive and Ohmic effects dominate. When $Re >> 1$ the plasma is highly conductive and flows freely, which is the case in the solar corona.

If we take the case of high resistivity the induction equation reduces to the standard diffusion. equation.

$$\frac{\partial \mathbf{B}}{\partial t} = \eta \nabla^2 \mathbf{B} \tag{2.10}$$

We can then estimate how the magnetic field decays over time taking the magnitudes of the both terms in the diffusion equation we get

$$\frac{B}{t_d} \approx \eta \frac{B}{L^2}$$

from this we can estimate the resistive diffusion time t_d. Using values for the corona, $L = 1000$ km, $T = 10^6$ K we get $t_d \approx 3 \times 10^6$ years. Thus in the corona we can normally neglect the diffusion of magnetic field lines.

It can now be seen that the continuity (2.1), Navier-Stokes (2.2), pressure (2.4) and induction equation (2.9) form a compatible set of equations known as the MHD equations with vectors $\mathbf{B}$, $\mathbf{v}$, p and scalars, ρ, T making up the 9 primary variables of MHD.

2.2 Ideal Magnetohydrodynamics

Hot plasmas, as is the case with the Sun, are very good conductors of electricity (Schnack [2009]). Hence a simplified version of MHD will be derived by ignoring R_v, $\mathbf{q}$ and setting resistivity $\eta = 0$, such that there is no magnetic diffusion. The assumption of no magnetic diffusion is justified as we previously showed t_d to be very large in the corona. Now an important result in ideal MHD known as the 'frozen flux theorem' will be shown and aid in helping understand the formation of magnetic structures in the corona.

First we start by writing an expression for the magnetic flux Φ, within a surface S with boundary C,

$$\Phi = \int_S \mathbf{B} \cdot d\mathbf{S} \tag{2.11}$$

next taking the time derivative of the flux which consists of two parts,

$$\frac{d\Phi}{dt} = \int_S \frac{\partial \mathbf{B}}{\partial t} \cdot d\mathbf{S} + \oint_C \mathbf{B} \cdot (\mathbf{v} \times d\mathbf{l}) \tag{2.12}$$

with the first term on the right hand side being the change in flux due to the change in $\mathbf{B}$ with the contour fixed. The second term on the right hand side is the change in flux due to the change in the contour C as it moves with the fluid (figure 2.1).

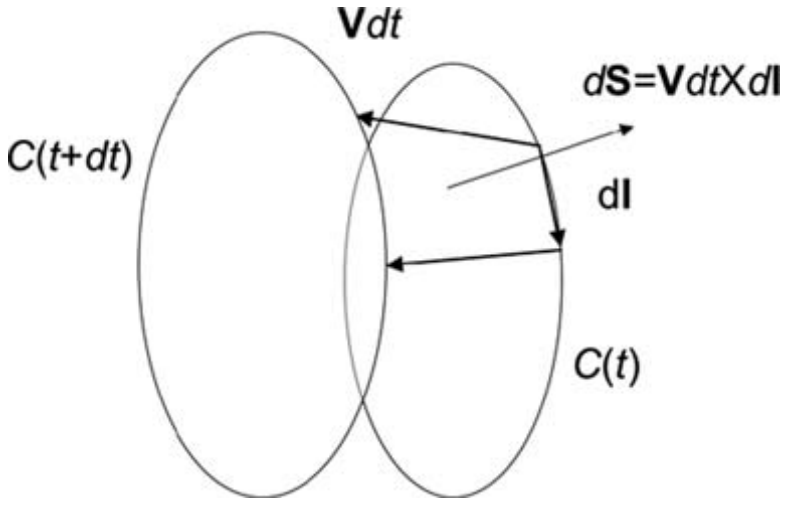

Figure 2.1: Surface element moving through fluid (Schnack [2009])

Then using Faraday's law and Stokes theorem the change in flux can be simplified.

$$\frac{d\Phi}{dt} = -\oint_C (\mathbf{E} + \mathbf{v} \times \mathbf{B}) \cdot d\mathbf{l}$$

Taking the ideal form of Ohm's law,

$$\mathbf{E} = -\mathbf{v} \times \mathbf{B} \tag{2.13}$$

it can then be seen that in ideal MHD that $\frac{d\Phi}{dt} = 0$. As a consequence of the frozen flux theorem it can be seen that the fluid is fixed to the field lines and hence cannot move across them (Schnack [2009],Priest [2012]). This is known as Alfvén's theorem after the pioneering founder of MHD, Hannes Alfvén.

2.3 Force-Free Fields and Flux Ropes

The corona can often be approximated to be in a state of equilibrium, neglecting gravity. Taking the momentum equation with at the steady state approximation (zero net force, $\mathbf{v}$ is constant), the Lorentz force and pressure gradient terms are such that

$$\mathbf{j} \times \mathbf{B} = \nabla p \tag{2.14}$$

using Ampere's law to get

$$\frac{1}{\mu_0}(\nabla \times \mathbf{B}) \times \mathbf{B} = \nabla p \tag{2.15}$$

finally using a standard vector identity we get

$$\frac{1}{\mu_0}(\mathbf{B} \cdot \nabla)\mathbf{B} = \nabla(p + \frac{B^2}{2\mu_0}) \tag{2.16}$$

(Golub and Pasachoff [2010]). In plasma physics the ratio of the two terms on the right hand side of (2.16) is the plasma beta.

$$\beta = \frac{2\mu_0 p}{B^2}$$

Taking typical values for the solar corona $B = 10^{-3}T$, $\rho = 10^{-13}kgm^{-3}$, $T = 10^6K$, giving $\beta = 10^{-3}$ and is even smaller around active regions. Hence thermal pressure is very small (compared to the magnetic pressure) and can be ignored. The corona is observed on average to be changing very slowly most of time, which along with small plasma-β gives rise to the force-free field condition.

$$\mathbf{j} \times \mathbf{B} = 0 \tag{2.17}$$

The force-free equation then leads to,

$$\frac{1}{\mu_0}(\nabla \times \mathbf{B}) \times \mathbf{B} = 0 \tag{2.18}$$

It then follows from the above condition that,

$$\nabla \times \mathbf{B} = \alpha \mathbf{B} \tag{2.19}$$

where α is a scalar function of position. Taking the divergence of (2.19) gives, $\mathbf{B} \cdot \nabla \alpha = 0$ showing α is a constant along each field line, where α is a function of position such that α can vary from one field line to another. Substituting Ampere's law into (2.19) it shows that the current is parallel to the magnetic field in a force-free field. Looking at the integral form of (2.19) it can be seen that α measures the magnitude of twist in the field (Golub and Pasachoff [2010]). It is sometimes convenient to assume α is constant in space, this is referred to as a constant-α field. Taking the curl of (2.19) with the constant-α assertion gives the spacial Helmholtz equation (2.20).

$$(\nabla^2 + \alpha^2)\mathbf{B} = 0 \tag{2.20}$$

Considering flux ropes for a moment as they are important coronal magnetic structures and understanding their geometry will be important moving forward. A coronal flux rope can be simplified into a flux tube by ignoring curvature (Figure 2.2), and easily modelled as a cylindrical force-free field as follows,

$$\frac{d}{dr}\left(\frac{B_\theta^2 + B_z^2}{2\mu_0}\right) + \frac{B_\theta^2}{\mu_0 r} = 0 \tag{2.21}$$

Where the field has θ and z components. The first term of (2.21) is the magnetic pressure and the second term is the magnetic tension force arising from curvature of the fields.

Solving the Helmholtz equation (2.20) by considering a cylindrical magnetic flux tube in which fields only depends only on the radius along the central axis of the flux tube, r gives,

$$r^2 \frac{d^2 B_\theta}{dr^2} + r\frac{dB_\theta}{dr} - (1 - \alpha^2 r^2)B_\theta = 0 \tag{2.22}$$

and

$$r^2 \frac{d^2 B_z}{dr^2} + r\frac{dB_z}{dr} + \alpha^2 r^2 B_z = 0 \tag{2.23}$$

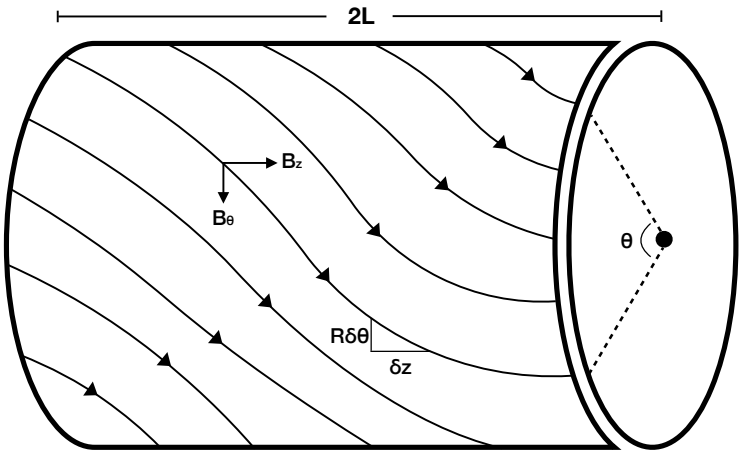

Figure 2.2: A twisted magnetic flux tube

the general solution to the force-free fields equations in cylindrical geometry can then be written as where the basis of the solutions to (2.22) and (2.23) are Bessel functions,

$$B_\theta = B_0 J_1(\alpha r) \tag{2.24}$$

$$B_z = B_0 J_0(\alpha r) \tag{2.25}$$

where J_1 and J_0 are Bessel functions of 1st and 0th order respectively (Figure 2.3). It must be noted that the above solutions to the differential equation are valid only for constant-α or linear force-free fields.

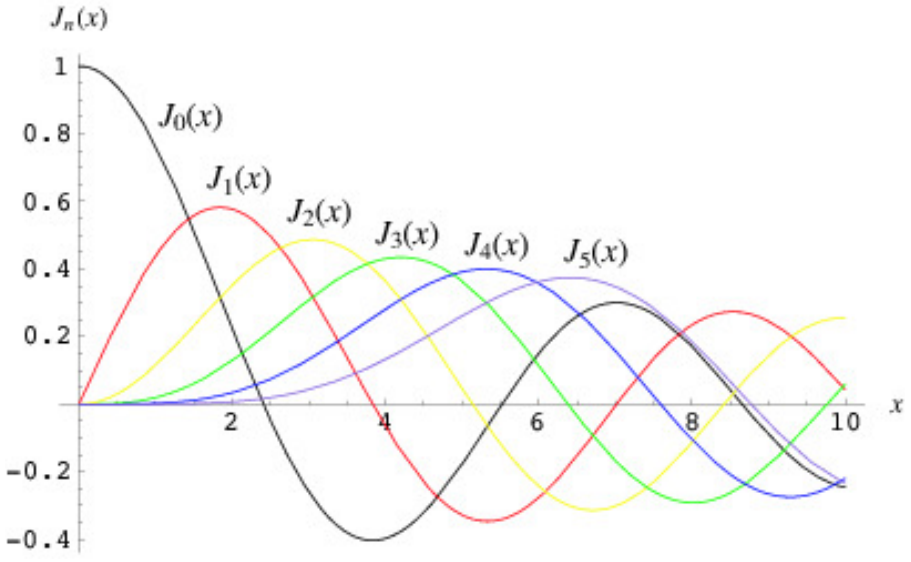

Figure 2.3: Graphical display of the Bessel functions which are solutions to Laplace's equation (EW Weisstein)

2.4 Magnetic Reconnection

For completeness we shall touch on magnetic reconnection, the mechanism by which the corona is thought to be heated, later we will see reconnection can be bypassed though the use of relaxation theory. Reconnection is still an evolving field of study, for more detail refer to Priest [2000], Gonzalez and Parker [2016] and MacTaggart and Hillier [2019].

Before diving into reconnection we first must describe why it is needed. In MHD, processes which convert magnetic energy into thermal-kinetic energy can be classified as ideal or non ideal. The difference between ideal and non ideal processes is the amount of energy released given and the timescale of energy release. In ideal processes energy released is relatively small and occurs very quick as the magnetic field is unable to dissipate adequately (t_d is large, section 2.1). While in non ideal processes can dissipate magnetic energy adequately into thermal energy, however are generally slower (Priest [2000]).

Solar flares can release stored magnetic energy in around 100 seconds, which is much faster than t_d in ideal processes such that a fast non-ideal mechanism must be found. Magnetic reconnection is a viable non ideal mechanism to dissipate magnetic energy into thermal energy. Magnetic reconnection can be defined as the change in field line topology when two oppositely directed field line components interact (Holman [2012]), converting stored magnetic energy into thermal energy (Figure 2.4 (a)). A thin current sheet arises on the area of reconnection where particles are accelerated (Figure 2.4 (a)). A simple explanation for this acceleration around current sheets is that as the fields move with the plasma and plasma density increases towards the currents sheet hence there exists a greater magnetic pressure, analogous to squeezing a tube of toothpaste with holes at both ends.

'One of the principle goals of reconnection theory is to explain how reconnection occurs on short enough timescale' (Priest [2000]). To achieve this goal two 2D models for recconnection were initially developed. One such model being the Sweet-Parker model (Parker [1957]) in which the current sheet at the reconnection site is as long as the global scale length of the region. However, dissipation times in solar flares were much shorter than predicted the by Sweet-Parker model and hence it is often referred to as slow reconnection. Later Petschek reconnection (Petschek [1964]) allowed for faster reconnection as the current sheet used is many orders of magnitude

smaller than in the Sweet-Parker model, allowing for a reconnection rate close to the rate needed in solar flares.

The standard model for solar flares has been built over many years (Figure 2.4). In the standard model a vertical current sheet forms as shown in Figure 2.4 (b). After a shear force is applied to the loops by photospheric foot point motion, reconnection interlinks the fields which are ejected towards the surface below the current sheet forming an arcade of loops. The field above the current sheet is pushed upwards and interlinks such that a magnetic flux rope forms (Figure 2.4 (c)) and eventually evolves into a CME.

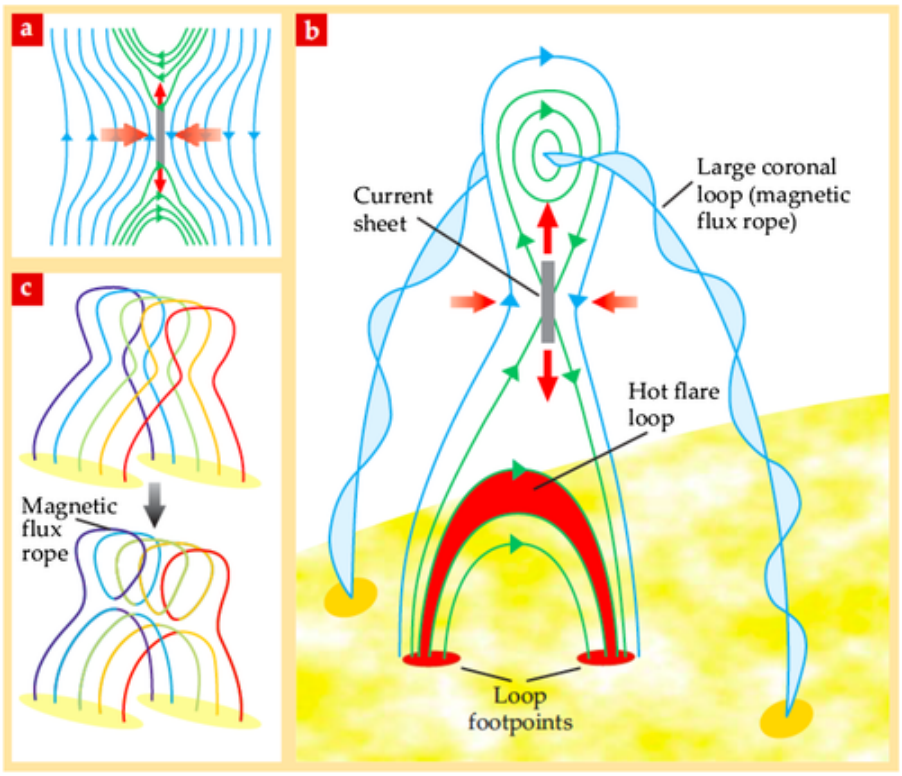

Figure 2.4: The Standard Model for the magnetic evolution of a solar flare. (a) The reconnection process, with in-flowing magnetic field in blue and out-flowing field in green. (b) Reconnection a larger context, producing the new flare arcade below and the magnetic flux rope above. (c) How the sheared arcade of loops reconnects to produce the flux rope and the less sheared flare arcade (Holman [2012]).

Chapter 3

Relaxation Theory and Magnetic Helicity

In order to understand DC coronal heating, as is the main focus of this text, an important frame work known as relaxation theory must be understood. Relaxation theory makes use of a global invariant in ideal MHD, a quantity known as magnetic helicity (section 3.1) which essentially measures self and mutual linkage between magnetic field lines.

Relaxation theory (Taylor [1974],Taylor [1986]) was developed to apply energy minimisation (section 3.2) techniques (Woltjer [1960]) to real plasma ($\eta \neq 0$). By knowing the properties of a plasma and its initial energy state the 'relaxed' lower energy state can be obtained. Relaxation theory is built upon Taylor's hypothesis (Taylor [1974]), which conjectures that; for a real plasma with low resistivity magnetic field lines can break as long as global helicity is approximately conserved over the entire plasma volume, however locally the helicity does not have to be conserved (section 3.3.3). Therefore the global magnetic helicity can be used as a constraint and results in the redistribution of magnetic helicity within the system. Taylor hypothesis postulates for the relaxation of magnetic fields by assuming a small localised regions of resistivity such that the magnetic fields are allowed to dissipate, releasing energy. Relaxation theory is a powerful tool to study plasma as it can bypass the complex intermediary interactions such as turbulence and reconnection. Hence, relaxation is much less computationally expensive than resistive 3D MHD models. The advantages of using relaxation theory also provide

its drawbacks. These include not having time dependant information required for a heating rate, such that a relaxation timescale has to be estimated from reconnection or numerically via resistive 3D MHD models (Lothian and Browning [2000]).

3.1 Helicity

To quantitatively understand relaxation models for coronal heating we must formulate our definition of helicity in flux tubes.

3.1.1 Definition of Helicity

Helicity K can be defined as,

$$K = \int_{V_0} \mathbf{A} \cdot \mathbf{B} \mathrm{d}V \tag{3.1}$$

where $\mathbf{A}$ is the vector potential defined by $\mathbf{B} = \nabla \times \mathbf{A}$. Here a topological description of helicity will be looked at (Schnack [2009], Berger [1999], Finn and Antonsen [1984]). Consider

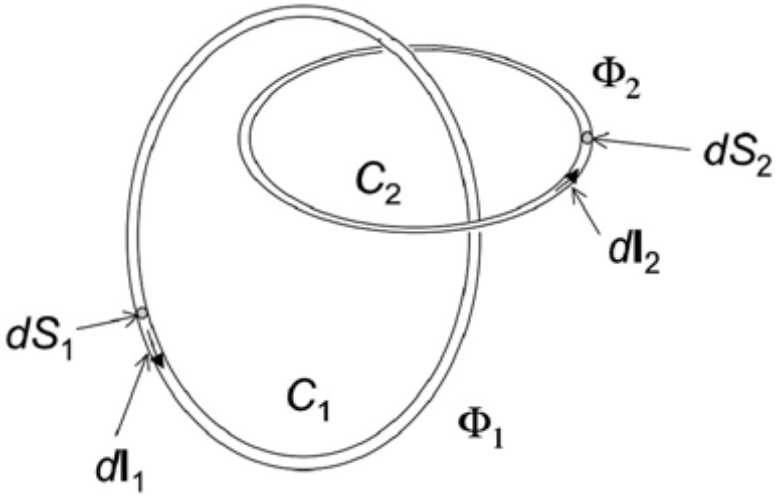

Figure 3.1: Interlinking flux tubes(Schnack [2009])

two linked flux tubes as in Figure 3.1. Tube C_1 has flux Φ_1 and tube C_2 has flux Φ_2. The helicity for C_1 can be written as

$$K_1 = \int_{S_1} \mathbf{B} \cdot \hat{\mathbf{n}} \mathrm{d}S \oint_{C_1} \mathbf{A} \cdot \mathrm{d}\mathbf{I} \tag{3.2}$$

in which case the first integral is the flux within C_1, Φ_1. The second integral is the flux enclosed by C_1, Φ_2. The flux Φ_2 is positive if the magnetic field is counter clockwise in C_2 and negative if clockwise, if there is no linkage then it is 0.

$$K_1 = \Phi_1 \Phi_2 \tag{3.3}$$

and

$$K_2 = \Phi_2 \Phi_1 \tag{3.4}$$

The total helicity can be more generally written as,

$$K = \sum_{i=1}^{N} \sum_{j=1}^{N} L_{ij} \Phi_i \Phi_j \tag{3.5}$$

where L_{ij} is the linking number, when $i \neq j$ it gives the mutual helicity, when $i = j$ the self helicity is obtained. To further understand self helicity it may be useful to integrate over (3.1) a single flux tube i to show L_{ii} equal to some average twist.

Helicity is a conserved quantity in ideal MHD and $\frac{dK}{dt} = 0$ is a consequence. Ideal MHD requires $\eta = 0$ such that reconnection is not allowed (field lines cannot be broken) as shown by the induction equation in section 2.3. 'Magnetic helicity in this sense is more robust than magnetic energy, as ideal motions convert energy back and forth between kinetic and magnetic forms' Berger [1999]. Energy minimisation using helicity conservation was first shown in Woltjer [1960] hence K is also known as the Woltjer invariant.

3.1.2 Helicity in Open Volumes

Note that the vector potential $\mathbf{A}$ is subject to an arbitrary choice of gauge. The previous description of helicity (3.1) is gauge invariant under the well known gauge transform $\mathbf{A} \rightarrow \mathbf{A} + \nabla\chi$ in a simply connected volume such as a sphere. However going forward we will use a more general form of helicity that satisfies the boundary conditions $\mathbf{B} \cdot \mathbf{n} = \mathbf{B_0} \cdot \mathbf{n}$ for an open volume, given as

$$K = \int_V (\mathbf{A} + \mathbf{A}_0) \cdot (\mathbf{B} - \mathbf{B_0}) \mathrm{d}V, \tag{3.6}$$

where $\mathbf{B_0}$ is the vacuum field ($\nabla \times \mathbf{B_0} = 0$) and $\mathbf{A_0}$ is the corresponding vector potential related via $\mathbf{B_0} = \nabla \times \mathbf{A_0}$ (Berger and Field [1984], Berger [1999],Finn and Antonsen [1984], Taylor [1986]). If the surface through which the field line penetrates has end points on the boundary, such as at the ends of a coronal loop then the linking of field lines definition of helicity (3.1)

breaks down.

3.2 Minimum Energy Theorem

The minimum energy theorem is the mathematical framework (Woltjer [1960]) from which we can calculate the energy release from discrete heating events (relaxations) using global helicity conservation. The magnetic fields in the corona can build up energy by turbulent phosphoric motion, upon reaching some critical value the field can relax to a lower energy state. The minimum energy theorem when combined with relaxation theory (global helicity conservation) allows us to calculate that minimum energy. We can then work out the energy released from a single relaxation event if we know the initial energy of the field.

The derivation goes as follows, we start with the Lagrangian of our system, where α is a constant known as the Lagrange multiplier (Schnack [2009]).

$$W = \frac{1}{2\mu_0}\int_{V_0}(\mathbf{B}^2 - \alpha\mathbf{A}\cdot\mathbf{B})dV \tag{3.7}$$

Minimising the integrad using the calculus of variation which requires varying the magnetic field and vector potential such that $\mathbf{A} \rightarrow \mathbf{A} + \delta\mathbf{A}$ and $\mathbf{B} \rightarrow \mathbf{B} + \delta\mathbf{B}$ with $\delta\mathbf{B} = \nabla \times \delta\mathbf{A}$ obtaining.

$$2\mu_0\delta W = \int_{V_0}(\mathbf{B}\cdot\delta\mathbf{B} - \alpha(\delta\mathbf{A}\cdot\mathbf{B} + \mathbf{A}\cdot\delta\mathbf{B}))dV \tag{3.8}$$

Using the divergence theorem and standard vector calculus identities, $\mathbf{B}\cdot\hat{\mathbf{n}} = \mathbf{0}$ at the boundary. Then setting $\delta W = 0$ gives

$$\nabla \times \mathbf{B} = \alpha\mathbf{B}$$

which is the same as (2.19), where α is now a constant. Therefore if the field has minimum energy with conserved helicity, it is a constant-α force-free field (Woltjer [1960]).

3.3 Relaxation Models of Solar Coronal Heating

Parker [1988] postulated that the corona could be heated by nano-flares occurring frequently enough to heat the corona. We will explore nanoflare heating with the framework of relaxation theory, mentioning some early models of DC coronal heating along the way (Heyvaerts and Priest [1984]) and then more recent two and three-layer models (Browning [2003], Bareford et al. [2010]). Next, we will determine the validity of Taylor minimum energy states, to discern whether the use relaxation theory is physical. Finally, we will use a theory involving mean-field MHD to describe coronal heating known as 'hyperdiffusion' (Van Ballegooijen and Cranmer [2008]).

3.3.1 Relaxation and Helicity in the Solar Corona

Heyvaerts and Priest [1984] first used relaxation theory to study the heating of coronal flux tubes via relaxation in the corona. Heating occurs as the flux tubes moved though multiple force-free equilibria satisfying $\nabla \times \mathbf{B} = \alpha \mathbf{B}$. In the paper an isolated curved flux tube is perturbed via an initially ideal MHD shear stress at footpoints of the flux tube. The difference between the energy of the perturbed field and initial constant-α was used to calculate the change in energy. As the model geometry was quiet complex the energy was only calculated to second order. Using reconnection models for dissipation rate the heating flux was found to be,

$$F_H = \frac{B^2 \upsilon \tau_d}{\mu_0 \tau_0} \tag{3.9}$$

where τ_0 is the timescale for footpoint of photospheric motion and τ_d is the dissipation time. Limitations of this study include the fact that it had a net current (or conducting walls) however this is not the case for coronal flux tubes. The use of relaxation theory in general only gives an upper bound for coronal heating as it is assumed all of the energy released from relaxation goes into heat. There are many studies using relaxation in the solar corona including, heating by braiding, merging and shearing of magnetic flux ropes (Hussain et al. [2017], Wilmot-Smith et al. [2011], Ji and Wang [2007], Heyvaerts and Priest [1992], Vekstein et al. [1991]).

3.3.2 Multi-Layer Models of Relaxation in Cylindrical Flux Ropes

The idea for a cylindrical flux tube model was put forward by Melrose et al. [1994] (Figure 3.2) in order to vary the magnetic field profile throughout the loop to better approximate coronal flux tubes. Later these cylindrical flux tube models were used with relaxation theory to help obtain rates for coronal heating (Browning [2003], Bareford et al. [2011]). One justification of using cylindrical flux tubes are the large observed aspect ratios of coronal loops. Cylindrical relaxation models have advantages over their curved counter parts (Heyvaerts and Priest [1984]) due to being able to be solved analytically and can have variable field profiles (Lothian and Browning [2000]). In addition a current neutralisation layer could be added to better approximate the profile of a coronal flux tube (Bareford et al. [2011]).

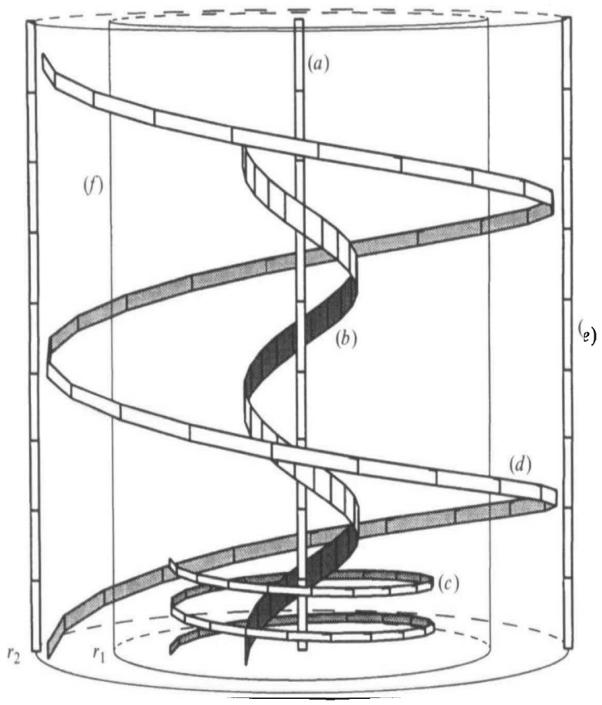

Figure 3.2: Representative magnetic field lines (a)-(e) for the two layer model. Each field line is followed for a twist through 4π Melrose et al. [1994].

Rather than a shear perturbation as in Heyvaerts and Priest [1984], in the cylindrical model energy is built up in the loop through coronal footpoint motion (Browning [2003],Browning et al. [2008]). Energy is released when the field becomes linearly unstable and the field crosses the threshold for ideal MHD instability known as a kink instability (Figure 3.3). After application of the kink displacement (right side Figure 3.3) the field is greater at A than B such that

a force further increases the perturbation. The energy is dissipated in the non-ideal phase of evolution of the instability due to fast recconnection and verified by simulation (Browning et al. [2008]).

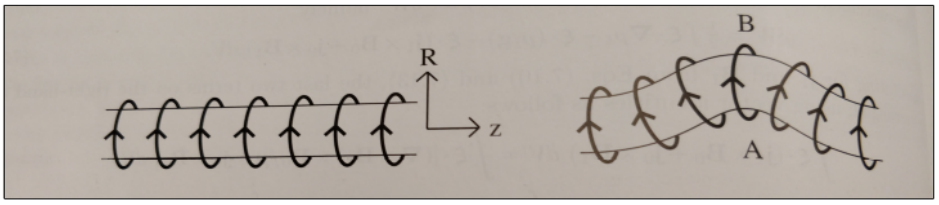

Figure 3.3: Left side, an equilibrium flux tube with azimuthal field lines tube. Right side, kink perturbation of the flux tube (Priest [2012])

From MHD simulation we know that ideal kink instability arises and leads to fine scale current structures in the non-linear phase of the instability (Browning et al. [2008]). The non linear effects allow for some resistivity for magnetic reconnection. The field then relaxes to a minimum energy state where α is constant.

In Browning [2003] a two layer model was developed using Bessel functions (section 2.3) to generate a series of force-free fields in each layer. The fields were then used with the gauge invariant definition of helicity (3.6) and integrated over the volume to give the total helicity. To obtain the energy the fields were integrated over the energy density of a magnetic field ($\frac{B^2}{2\mu_0}$), then final expressions for the energy was obtained. Finally, assuming helicity conservation the relaxed constant α value can be found and used to calculate the energy release.

Results from Browning [2003] showed that a minimum size for a discrete heating event could be obtained, with smaller events being more common. After performing multiple relaxations with alpha values chosen inline with stability analysis, the energy range for heating events was found to be between $10^{18} - 10^{20}$J. A heating rate was found using numerical relaxation timescales and was found to be adequate for coronal heating. Limitations of this work include not including curvature hence the loops will have a lower energy (no magnetic tension). The inaccurate assumption of a conducting wall was also used.

Bareford et al. [2011] extended this model by using three layers, with the last layer being a neutralisation layer, such that the flux tube had zero net current. The calculation for energy

release was the same as Browning [2003], however this time an ensamble of loops was relaxed to obtain a distribution of heating events. The loop aspect ratio was also varied. In the end the heating rate obtained was also sufficient for coronal heating.

3.3.3 Evidence for and Against Taylor Minimum Energy States

To first understand the validity of using Taylor's theorem we must first take a deeper look into the assumptions made; that the relaxation of the plasma is caused by resistivity on small length scales, leading to the dissipation of magnetic energy even though this strictly not true in ideal systems.

In order to account for dissipative effects we must consider the non turbulent resistive plasma such that;

$$\frac{dK}{dt} = -2\eta \int \mathbf{j} \cdot \mathbf{B} dV \tag{3.10}$$

and

$$\frac{dW}{dt} = -\eta \int j^2 dV \tag{3.11}$$

Where the decay rate of K and W is same. However, when considering resistive (η is large) turbulent plasma we can take into account small scale fluctuations with wave vector, $\mathbf{k}$ in Fourier space such that $\mathbf{B} = \sum \mathbf{B_k} e^{i\mathbf{k}\cdot\mathbf{r}}$ and $\mathbf{J} = \sum i\mathbf{k} \times \mathbf{B_k} e^{i\mathbf{k}\cdot\mathbf{r}}$ giving;

$$\frac{dK}{dt} \approx -2\eta \sum |\mathbf{k}| {\mathbf{B_k}}^2 \tag{3.12}$$

and

$$\frac{dW}{dt} \approx -\eta \sum \mathbf{k}^2 {\mathbf{B_k}}^2 \tag{3.13}$$

for further derivation details see Schnack [2009] and Qin et al. [2012]. From (3.12) and (3.13) we can see that during relaxation W decays as $\mathbf{k}^2$ and K decays as $\mathbf{k}$. If the relaxation process is dominated by structures with wavelengths shorter than $\eta^{\frac{1}{2}}$, dissipation of W will be more efficient than than that of K.

Evidence of small scale turbulent structures is needed to verify the evolution of fields to a Taylor minimum energy state, but as Taylor envisaged is difficult to obtain. Some numerical

resistive MHD simulations show Taylor relaxation states (Browning et al. [2008], Hood et al. [2009]), while others show global helicity conservation but not the final constant-α state (Yeates et al. [2010], Amari and Luciani [2000]). It was also shown mathematically that the Taylor relaxation state could be obtained without Taylor's hypothesis, at all wavelengths (Qin et al. [2012]). Observationally, there has been some evidence of Taylor relaxed states in the corona (Nandy et al. [2004]).

3.4 Helicity Transfer and Alpha Profiles

An idea was proposed for the heating coronal flux ropes using mean-field MHD and self consistent turbulence, through an effect coined as 'hyperdiffusion' (Van Ballegooijen and Cranmer [2008]). In hyperdiffusion, stochastic magnetic fields within a flux rope are diffused while preserving helicity and may also provide an explanation for fast reconnection in the corona. Hyperdiffusion can then be used to describe how the magnetic system relaxes to a Taylor state. The mathematical framework of hyperdiffusion was developed by Boozer [1986], Bhattacharjee and Hameiri [1986]. We will now summarise key results for this theory as related to the helicity transfer and energy release. To obtain relationships for the transfer of helicity we start with the evolution of the vector potential

$$\frac{\partial \mathbf{A}}{\partial t} = -c\mathbf{E} - \nabla\phi \tag{3.14}$$

where $\mathbf{B}(\mathbf{r}, t)$ is the sum of mean and fluctuating components of the field and $\mathbf{A} = \nabla \times \mathbf{B}$, $\phi(\mathbf{r}, t)$ is the scalar potential. Using Ampere's and Ohm' law we then get

$$\frac{\partial \mathbf{A}}{\partial t} = -\mathbf{v} \times \mathbf{B} - \eta \times \nabla\mathbf{B} - \nabla\phi \tag{3.15}$$

where $\mathbf{v}(\mathbf{r}, t)$ is the plasma velocity. The magnetic helicity equation can be obtained from (3.15)

$$\frac{\partial}{\partial t}(\mathbf{A} \cdot \mathbf{B}) + \nabla \cdot K = -2\eta\mathbf{B} \cdot \nabla \times \mathbf{B} \tag{3.16}$$

the helicity density is given by $(\mathbf{A} \cdot \mathbf{B})$ and the helicity flux $K(\mathbf{r}, t)$ is defined as

$$K \equiv \mathbf{A} \times (-c\mathbf{E} + \nabla\phi). \tag{3.17}$$

Next we introduce $\mathbf{B}_0(\mathbf{r}, t)$ as the mean magnetic field smoothed over an intermediate length

scale l and the fluctuating field is $\mathbf{B}_1(\mathbf{r}, t)$ on length scales less than l, following the calculation in Van Ballegooijen and Cranmer [2008] the equation for the evolution of the vector potential (3.15) can be reconstructed using these two quantities ($\mathbf{B}_0$, $\mathbf{B}_1$) to give the contributions of the fluctuations to the helicity flux K_0 and is defined as

$$K_0 \equiv \langle \mathbf{A} \times (-c\mathbf{E}_1 + \nabla\phi_1) \rangle. \tag{3.18}$$

The relationship between the fluctuations of the helicity flux and the mean electromotive force (EMF) ϵ_0 is found to be

$$2\epsilon_0 \cdot \mathbf{B}_0 = -\nabla \cdot K_0. \tag{3.19}$$

The EMF can be decomposed into components $\epsilon_0 = \epsilon_{0,||} + \epsilon_{0,\perp}$ and the parallel component can be obtained from (3.19). It was assumed that the helicity budget is dominated by large scale structure such that total helicity is equal to the mean field helicity. The fluctuating helicity flux for a linear force-free field (constant α_0) should be zero as there is no free energy to drive the fluctuations, following Boozer [1986] and Bhattacharjee and Hameiri [1986] it's assumed $K_0 \propto \nabla\alpha_0$ such that;

$$K_0 = -2\eta_4 B_0^2 \nabla\alpha_0. \tag{3.20}$$

Where B_0 is the magnitude of the mean magnetic field and can be related to α_0 (torsional parameter of mean-field) by $\nabla \times \mathbf{B}_0 = \alpha_0 \mathbf{B}_0$ and η_4 is the hyperdiffusivity. Equation (3.20) can then be used with mean field evolution of the vector potential, EMF and the force-free condition (see Bhattacharjee and Hameiri [1986], Boozer [1986]), to get the energy equation for the mean magnetic field;

$$\frac{\partial}{\partial t}\left(\frac{B_0^2}{8\pi}\right) + \nabla \cdot \left(\frac{B_0^2}{4\pi}\mathbf{v}_0 - \eta_4 \frac{B_0^2}{4\pi}\alpha_0 \nabla\alpha_0\right) = -\eta_4 \frac{B_0^2}{4\pi}|\nabla\alpha_0|^2 \tag{3.21}$$

where $\mathbf{v}_0 = \mathbf{v}_0' + \mathbf{u}_0$ which is the total transport velocity, transport velocity $\mathbf{u}_0$ is defined as $\mathbf{u}_0 \equiv (\mathbf{B}_0 \times \epsilon_{0,\perp})/B_0^2$ and $\mathbf{v}_0'$ is the mean plasma velocity. The term on the right hand side of (3.21) is negative and can be seen as the rate at which the mean field is converted to heat.

The effect of hyperdiffusion can be said to depend on $\nabla\alpha_0$ and can be used to describe the tendency of the field to relax. Small scale reconnection events can be shown to produce a net

helicity flux, K_0. The spatially averaged heating rate is shown to be proportional to $|\nabla\alpha_0|^2$ equation (3.21), while the the fluctuation (change relative to the average) of helicity K_0 is proportional to $\nabla\alpha_0$. Moving forward we will compare the relationships obtained for coronal heating by hyperdiffusion (equations (3.20), (3.21)), to those of multi-layer cylindrical relaxation models.

Chapter 4

Multi-Layer Cylindrical Models of Coronal Loops

Next we will build upon work done previously on cylindrical relaxation models by Browning [2003] and Bareford et al. [2011] and extend the model up to any arbitrary number of layers. All programs used to calculate the multi-layer helicity, relaxation energy and field profiles values have been coded myself in Python. Packages used to build the code include NumPy, SciPy and Matplotlib. A large part of the project involved creating the code, along with the many checks required to confirm its validity as discussed later in the text.

The main reasons to extend previous models include; the ability to generate any arbitrary field profile, almost continuously within flux tubes when the number of layers is large. Better approximation of field profiles allow for more accurate values of for energy and helicity. The multi-layer code developed also allows for the relaxation of non analytic field profiles to be calculated such as in Hood et al. [2009] (equations (4.9), (4.10),(4.11)).

4.1 Magnetic Fields

An idealised model of a straight cylindrical flux tube is used to represent the photosphere at $z = 0, L$ (Browning [2003]). Photospheric footpoint motion can then twist the fields within the flux tube. In the model, the number of layers in cylindrical flux tube can be specified up any number of layers (Figure 4.1), where each layer has a different specified value of $\alpha(r)$ (piece-wise continuous), while the magnetic field is continuous at the boundaries. For simplicity the maximum radius of the flux tube is normalised to 1. It must be noted that even though this model is simplified the same physical processes should apply to more intricate geometries.

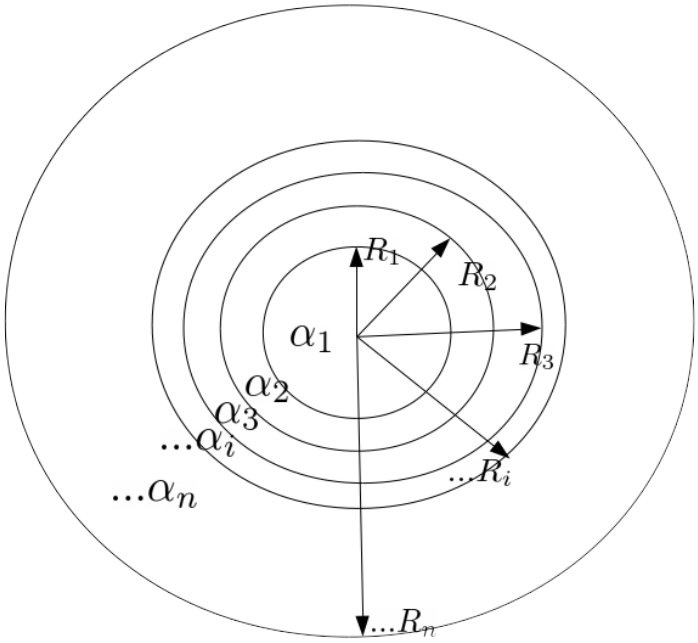

Figure 4.1: Top down view of cylindrical model, with an the arbitrary number of layers with R_i and α_i. The layer with the largest radius, $R_n = 1$.

The magnetic field within the cylindrical flux tube will be such that it is continuous everywhere. In section 2.3 on force-free fields, it was found that the values of magnetic fields for flux tube in the corona can be found using Bessel functions. Similarly in our model the magnetic fields can be given as;

$$B_{1z} = B_1 J_0(|\alpha_1|r) \tag{4.1}$$

$$B_{1\theta} = B_1 J_1(|\alpha_1|r), \qquad 0 \leq r \leq R \tag{4.2}$$

$$B_{iz} = B_i J_0(|\alpha_i|r) + C_i Y_0(|\alpha_i|r) \tag{4.3}$$

$$B_{i\theta} = \sigma_i(B_i J_1(|\alpha_i|r) + C_i Y_1(|\alpha_i|r)), \qquad R_{i-1} \leq r \leq R_i \tag{4.4}$$

Where the general constants B_i, C_i are determined from B_1 (the value of the axial field at $r = 0$), using the fact the the fields are continuous across boundaries. Through-out the calculations $i \geq 2$ will be used for determining quantities such as the magnetic field between any adjacent layer other than the first, which is a special case. After matching across the boundary the constants obtained generally are;

$$B_i = \frac{\pi R_{i-1} B_{i-1}|\alpha_i|}{2}(\sigma_{i-1,i} F_1^{i-1}(|\alpha_{i-1}|R_{i-1})Y_0(|\alpha_i|R_{i-1}) - F_0^{i-1}(|\alpha_{i-1}|R_{i-1})Y_1(|\alpha_i|R_i)) \tag{4.5}$$

$$C_i = \frac{\pi R_{i-1} B_{i-1}|\alpha_i|}{2}(F_0^{i-1}(|\alpha_{i-1}|R_{i-1})J_1(|\alpha_i|R_{i-1}) - \sigma_{i-1,i} F_1^{i-1}(|\alpha_{i-1}|R_{i-1})J_0(|\alpha_i|R_{i-1})) \tag{4.6}$$

to allow for both positive and negative values for α, the sign of α_i is introduced as $\sigma_i = \frac{\alpha_i}{|\alpha_i|}$. To simplify the form of the equations (4.5) and (4.6) the following Bessel relationship is used;

$$Y_0(\alpha_i R_{i-1})J_1(\alpha_i R_{i-1}) - Y_1(\alpha_i R_{i-1})J_0(\alpha_i R_{i-1}) = \frac{2}{\pi|\alpha_i|R_{i-1}}. \tag{4.7}$$

To simplify calculations $F_{0,1}^i$ is introduced and given as;

$$F_{0,1}^i(x) = J_{0,1}(x) + \gamma_i Y_{0,1}(x) \tag{4.8}$$

where $\gamma_i = \frac{C_i}{B_i}$. We normalise all fields with respect to the axial flux ψ^* the which will be conserved during relaxation;

$$\begin{aligned}\psi^* &= \int_0^{R_i} 2\pi r^* B_z^* dr^* \\ &= 2\pi B_1 R_1 J_1(|\alpha_1|R_1)\left(\frac{1}{|\alpha_1|} - \frac{\sigma_{1,2}}{|\alpha_2|}\right) \\ &+ 2\pi \sum_{i=2}^{n} \frac{B_i}{|\alpha_i|}\left(R_i F_1^i(|\alpha_i|R_i) - R_{i-1}F_1^i(|\alpha_i|R_{i-1})\right)\end{aligned} \tag{4.9}$$

then we normalise B_1 by making $\psi^* = 1$ and rearranging. Upon obtaining B_1 the constants (4.5), (4.6) are recalculated and normalised.

Example Magnetic fields

We now take a slight detour from methodology, to analyse a useful field configuration, allowing the reader to better visualise our model.

A zero net current, force-free field configuration is used in Hood et al. [2009] as follows and is defined for $0 \leq r < 1$;

$$B_\theta = \lambda r(1 - r^2)^3 \tag{4.10}$$

$$B_z = \left(1 - \frac{\lambda^2}{7} + \frac{\lambda^2}{7}(1 - r^2)^7 - \lambda^2 r^2(1 - r^2)^6\right)^{\frac{1}{2}} \tag{4.11}$$

$$\alpha = \frac{2\lambda(1 - r^2)^2(1 - 4r^2)}{B_z} \tag{4.12}$$

where λ is a constant parameter chosen such that B_z^2 remains positive. When taking the limit as $r \to 1$ it can be seen $\alpha \to 0$ and $B_\theta \to 0$. Resistive MHD simulations were used to perform relaxations on a non analytic α profile (equations (15) in Hood et al. [2009]), however another way to calculate energy release is to use the multi-layer model we have developed. The approximate field profiles are given in Figure 4.4 and Figure 4.5 using the multi-layer model. The approximate field profiles can be seen as similar to the continuous field profiles and was an important check moving forward.

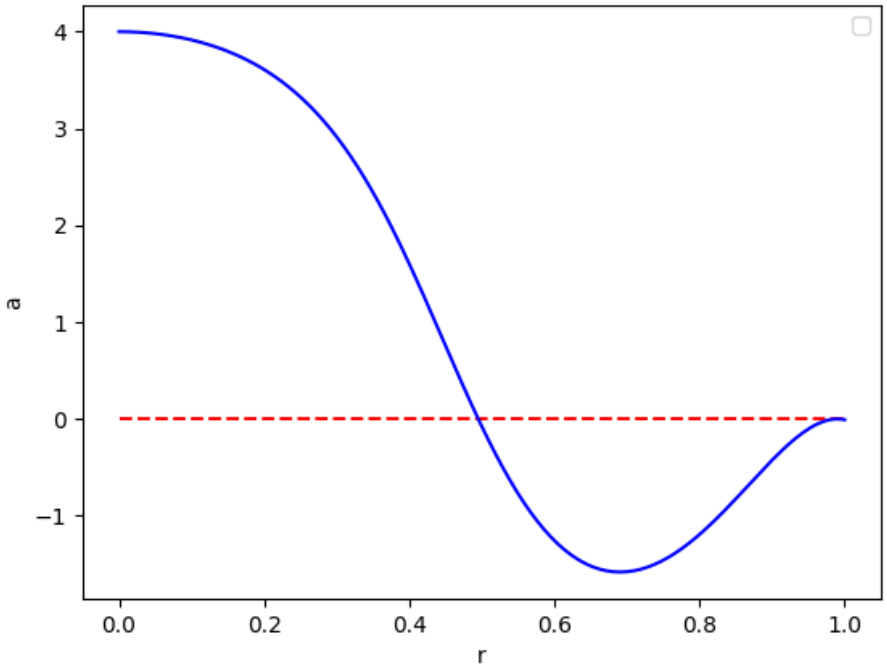

Figure 4.2: Hood et al. [2009] α profile.

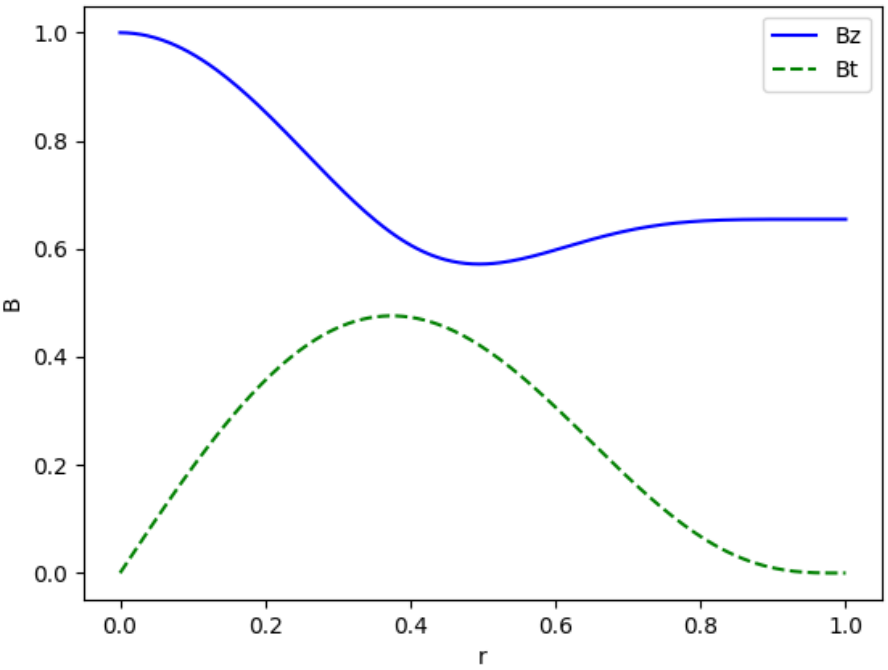

Figure 4.3: Axial and azimuthal field profiles from Hood et al. [2009].

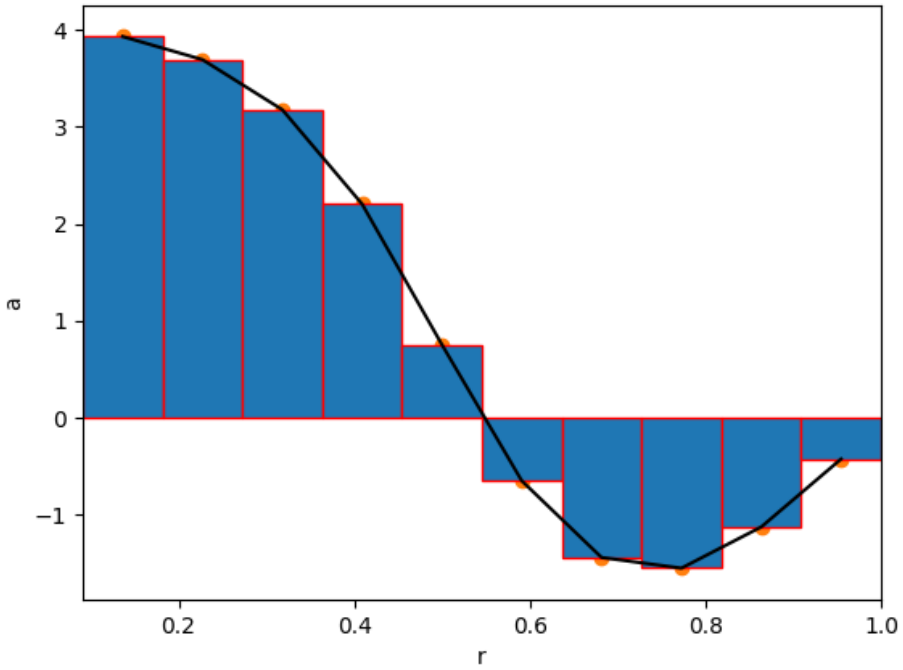

Figure 4.4: Approximate α profile generated from mutli-layer code to replicate Hood et al. [2009]. Where each bar represents a layer, n=10.

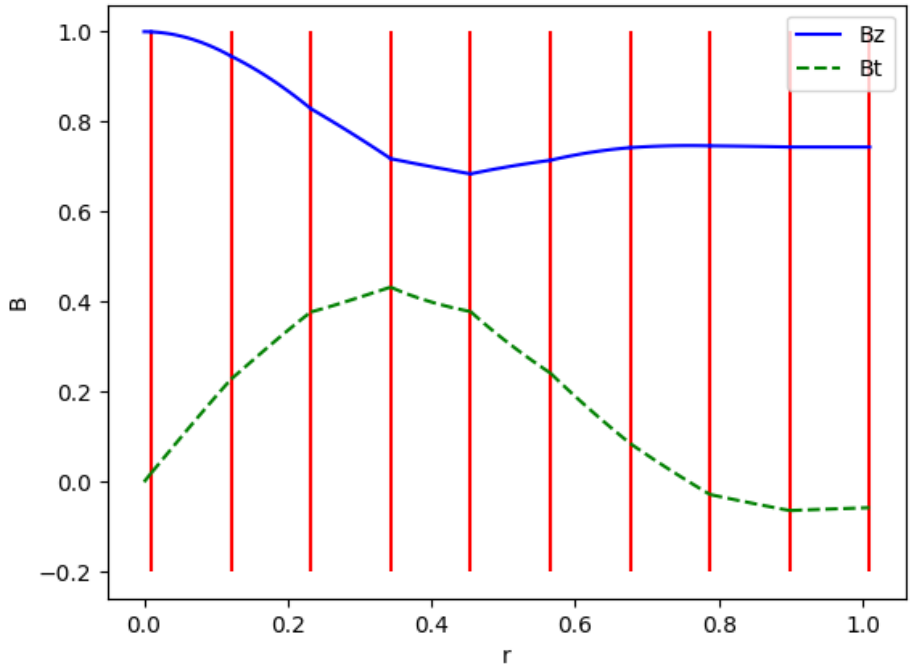

Figure 4.5: Approximation of axial and azimuthal field profiles from Hood et al. [2009]. Multi-layer code used for n=9 layers to generate plot, red vertical lines mark layer boundary.

4.1.1 Calculating Helicity and Energy

The energy and helicity in our model can be calculated by first using the axisymmertic fields as $\mathbf{B} = \frac{1}{2\pi r}\nabla\psi \times \hat{\theta} + \frac{I}{r}\hat{\theta}$ and $\mathbf{A} = \frac{1}{2\pi r}\psi\hat{\theta} + \mathbf{A}_\perp$ where $\mathbf{A}_\perp$ has only z and r components. The axial current can be written as $\frac{I}{\mu_0}$ and $\mathbf{I'} = 0$ as $\mathbf{B'}$ has no azimuthal component. The vacuum field and potential are given as $\mathbf{B'} = \frac{1}{2\pi r}\nabla\psi' \times \hat{\theta}$ and $\mathbf{A'} = \frac{1}{2\pi r}\psi'\hat{\theta} + \mathbf{A'}_\perp$. Following from Browning [2003], Bareford et al. [2011] and using the gauge invariant helicity as in section 3.1.2,

$$K = \int_V (\mathbf{A} + \mathbf{A'}) \cdot (\mathbf{B} - \mathbf{B'})\mathrm{d}V$$

giving,

$$K = 2\int_V \frac{I\psi}{2\pi r^2}dV + \int_V (\mathbf{A}_\perp + \mathbf{A'}_\perp) \cdot \nabla \times [(\psi - \psi')\hat{\theta}]dV \tag{4.13}$$

using the boundary conditions $\mathbf{B} \cdot \hat{\mathbf{n}} = \mathbf{B'} \cdot \hat{\mathbf{n}}$ and some rearrangement we get;

$$K = 2\int_V \frac{I\psi}{2\pi r^2} = 2L\int_0^R \frac{I\psi}{r}dr. \tag{4.14}$$

Now using the appropriate Bessel functions (equations (4.1), (4.2), (4.3) and (4.4)) to obtain the current I (Ampere's law) and axial flux, ψ (equation (4.9)), then integrating (using Bessel identities) radially over n-layers and setting $L = 1$, gives a general n-layer helicity;

$$K = K_{R_0}^{R_1} + \sum_{j=2}^{n} K_{R_{j-1}}^{R_j} \tag{4.15}$$

where (4.11) can be seen as summing the helicity of each layer to obtain the total helicity and $K_{R_0}^{R_1}$, $K_{R_{j-1}}^{R_j}$ are given as;

$$K_{R_0}^{R_1} = \sigma_1 \frac{2\pi L B_1^2}{|\alpha_1|}\left(R_1^2\big(J_0(|\alpha_1|R_1)^2 + J_1(|\alpha_1|R_1)^2\big) - 2\frac{R_1}{|\alpha_1|}J_0(|\alpha_1|R_1)J_1(|\alpha_1|R_1)\right) \tag{4.16}$$

$$
\begin{aligned}
K_{R_{j-1}}^{R_j} = \sigma_j \frac{2\pi L B_j^2}{|\alpha_j|} \Bigg(& R_j^2 \big(F_0^j(|\alpha_j|R_j)^2 + F_1^j(|\alpha_j|R_j)^2\big) - 2\frac{R_j}{|\alpha_j|} F_0^j(|\alpha_j|R_j) F_1^j(|\alpha_j|R_j) \\
& + R_{j-1}^2 \big(F_0^j(|\alpha_2|R_{j-1})^2 + F_1^j(|\alpha_j|R_{j-1})^2\big) - 2\frac{R_{j-1}}{|\alpha_j|} F_0^j(|\alpha_j|R_{j-1}) F_1^j(|\alpha_j|R_{j-1}) \Bigg) \\
& + \sigma_j \frac{4\pi L B_j}{|\alpha_j|} \Bigg(F_0^j(|\alpha_j|R_{j-1}) - F_1^j(|\alpha_j|R_j) \Bigg) \\
& \left[\sum_{i=1}^{j-1} B_i R_i F_1^i(|\alpha_i|R_i) \left(\frac{1}{|\alpha_i|} - \frac{\sigma_{i,i+1}}{|\alpha_{i+1}|} \right) \right]
\end{aligned}
\tag{4.17}
$$

where the summation term in (4.17) is a gauge correction as the helicity between layers is not additive. It can be seen that when there is only one unique value of helicity, such that $\alpha_1 = \alpha_2 = ...\alpha_{n-1} = \alpha_n$ the helicity for a single layer can be obtained as;

$$
K_{single} = \frac{2\pi L B^2}{|\alpha|} \left(R^2 \big(J_0(|\alpha|R)^2 + J_1(|\alpha|R)^2\big) - 2\frac{R}{|\alpha|} J_0(|\alpha|R) J_1(|\alpha|R) \right) \tag{4.18}
$$

which will be used later when calculating energy release from a relaxation event. When having only two unique values of helicity in (4.14) it is possible obtain the equations for the two layer model from Browning [2003]. The same can be seen for three unique values and the three layer model in Bareford et al. [2010]. These reductions will form an important part of the checks used when developing the code later on.

Similarly we can calculate the energy by integrating the energy density;

$$
W = \int_V \frac{B^2}{2\mu_0} dV \tag{4.19}
$$

with our Bessel function relations (4.1), (4.2), (4.3) and (4.4) for the magnetic field to obtain a general relation for the energy;

$$
W = W_{R_0}^{R_1} + \sum_{j=2}^{n} W_{R_{j-1}}^{R_j} \tag{4.20}
$$

where similarly to helicity, the total energy of the field in our model is given by (4.16) and $W_{R_0}^{R_1}$, $W_{R_{j-1}}^{R_j}$ are given as;

$$W_{R_0}^{R_1} = \frac{\pi L B_1^2}{\mu_0}\left(R_1^2\big(J_0(|\alpha_1|R_1)^2 + J_1(|\alpha_1|R_1)^2\big) - \frac{R_1}{|\alpha_1|}J_0(|\alpha_1|R_1)J_1(|\alpha_1|R_1)\right) \tag{4.21}$$

$$\begin{aligned} W_{R_{j-1}}^{R_j} = \frac{\pi L B_j^2}{\mu_0}\Bigg(& R_j^2\big(F_0^j(|\alpha_j|R_j)^2 + F_1^j(|\alpha_j|R_j)^2\big) - \frac{R_j}{|\alpha_j|}F_0^j(|\alpha_j|R_j)F_1^j(|\alpha_j|R_j) \\ & - R_{j-1}^2\big(F_0^j(|\alpha_2|R_{j-1})^2 + F_1^j(|\alpha_j|R_{j-1})^2\big) + \frac{R_{j-1}}{|\alpha_j|}F_0^j(|\alpha_j|R_{j-1})F_1^j(|\alpha_j|R_{j-1})\Bigg) \end{aligned} \tag{4.22}$$

similarly to helicity, that when there is only one unique value of α, the energy for a single straight cylinder can be obtained from (4.20) as;

$$W_{single} = \frac{\pi L B^2}{\mu_0}\left(R^2\big(J_0(|\alpha|R)^2 + J_1(|\alpha|R)^2\big) - \frac{R}{|\alpha|}J_0(|\alpha|R)J_1(|\alpha|R)\right) \tag{4.23}$$

again it can be seen that the two or three layer energy can be obtained from (4.19) depending on the number of unique values for α, in all calculations $L = 1$.

4.1.2 Calculating Energy Release

Using the previous expressions for helicity and energy we can now calculate the energy release during a single relaxation event. From Taylor's Hypothesis we know that the total helicity must be conserved, allowing us to find α for the relaxed state. Given some initial preset α values for our system we can find the total helicity. Next, we can use a root finding algorithm to solve;

$$K_{single}(\alpha) - K(\alpha_1, \alpha_2, ..., \alpha_n) = 0 \tag{4.24}$$

finding the value for the constant-α relaxed state, where $\alpha = \alpha(\alpha_1, \alpha_2, ..\alpha_n)$. An example of this root finding can be shown in Figure 4.6.

Once α for the relaxed state has been found the energy released can be then found according to;

$$\delta W = W(\alpha_1, \alpha_2, ..., \alpha_n) - W_{single}(\alpha) \tag{4.25}$$

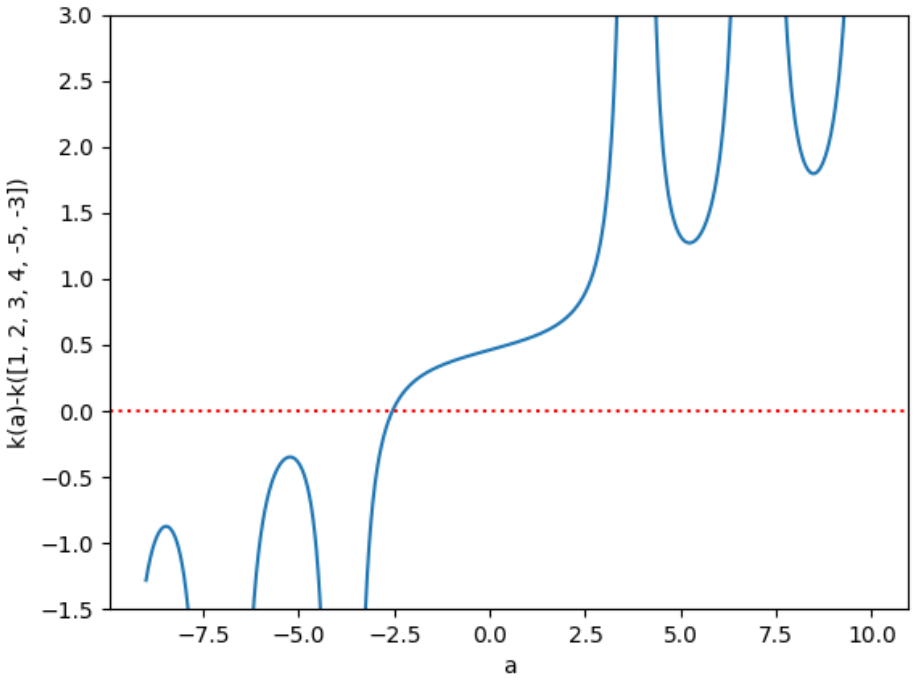

Figure 4.6: Showing the root (relaxed value of α) used to solve equation (4.23). Where in this case, a 6 layer cylindrical model was used as an example.

where initial energy is then subtracted from the final energy according giving the energy released.

Moving forward it may prove helpful to provide a practical example of how the energy release is calculated. To understand equation (4.25) we can first plot the energy in the case of a single layer (Figure 4.7). Interestingly it can be seen that the energy for a single layer varies similar to energy levels in an atom with successive 'wells' at higher energy. Continuing with the analogy to atomic energy levels, the lowest well in Figure 4.7 can be seen as the ground state. In Figure 4.8 it can be seen that if the relaxed value for α are outside the range for our minimum energy state δW becomes negative, hence we limit our root finding algorithm to the first 'well' in Figure 4.7.

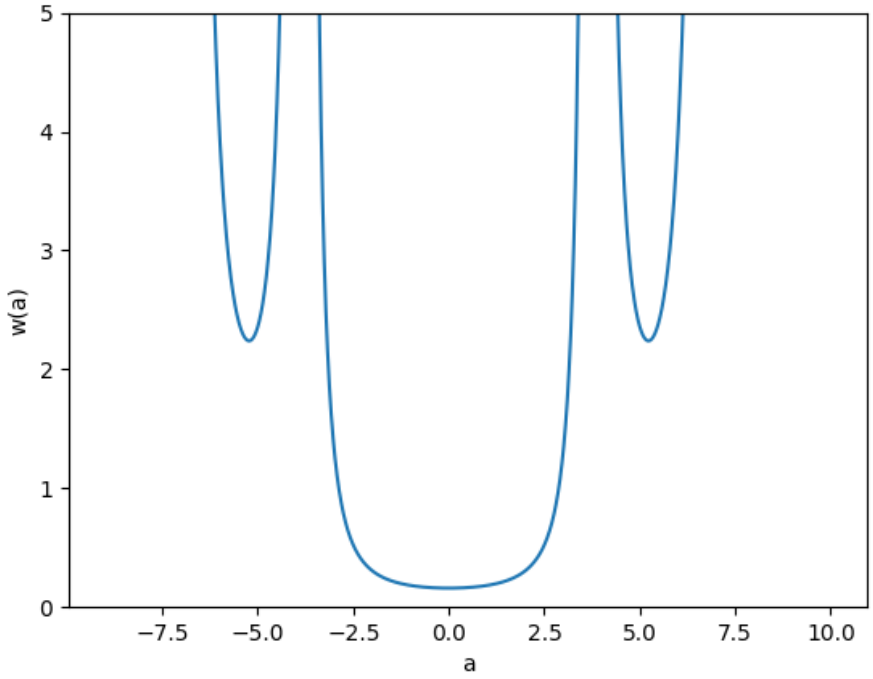

Figure 4.7: Showing how the energy $W_{single}(\alpha)$, varies.

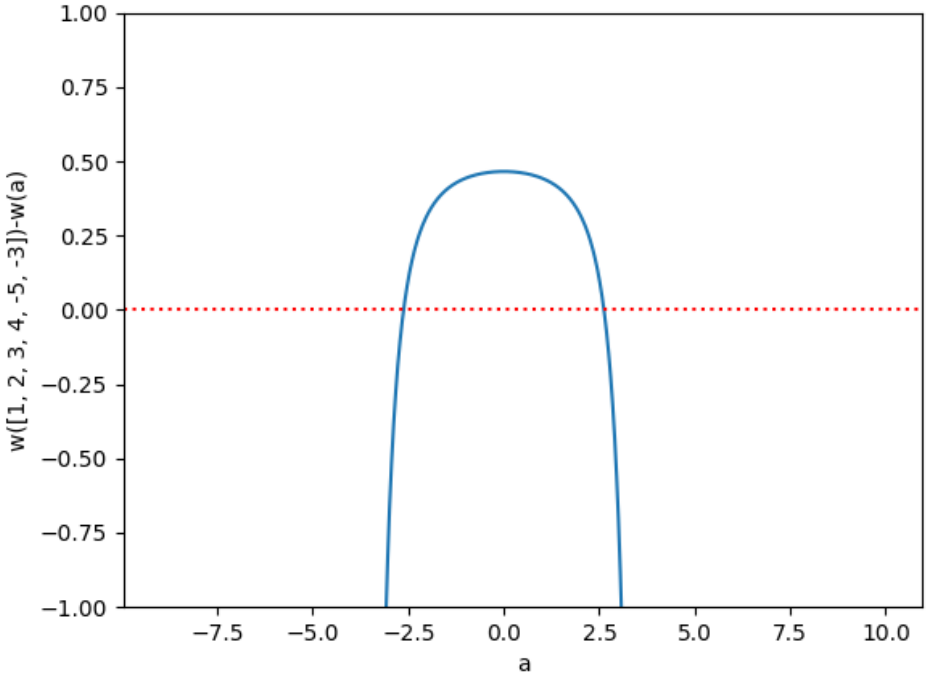

Figure 4.8: Showing how the energy released $\delta W(\alpha)$ similar to equation (4.24), varies, Again in this case, a 6 layer cylindrical model was used with the same α values as in Figure 4.4.

Chapter 5

Heating in Cylindrical Multi-Layer Loops: Results

In this chapter the results of energy release will be presented and compared to results from coronal heating by hyperdiffusion (Van Ballegooijen and Cranmer [2008]). The results from the multi-layer model will also be used to determine the accuracy of previously used two and three layer models from (Browning [2003], Bareford et al. [2011]). However, first we will discuss the checks performed on the code to determine the validity of the model before moving forward.

5.1 Testing Codes

In determining the validity of the multi-layer code many checks had to be performed. First we built a model of the helicity for of a single layer and then increased the complexity of the code to calculate the helicity for two, three, and then any number of layers. Helicity was used as the main comparison between models of different order as equations for helicity and energy are similar and from which the energy values could be easily could be obtained. Also if values for helicity are found to be correct, that also means that all the constants and normalisation values must also be correct. Before moving on to code higher order models, the helicity was compared with that of lower order models to assure accuracy.

Initially a helicity profile for a single layer was generated, as this was the simplest model it was easiest to confirm its validity (Figure 5.1).

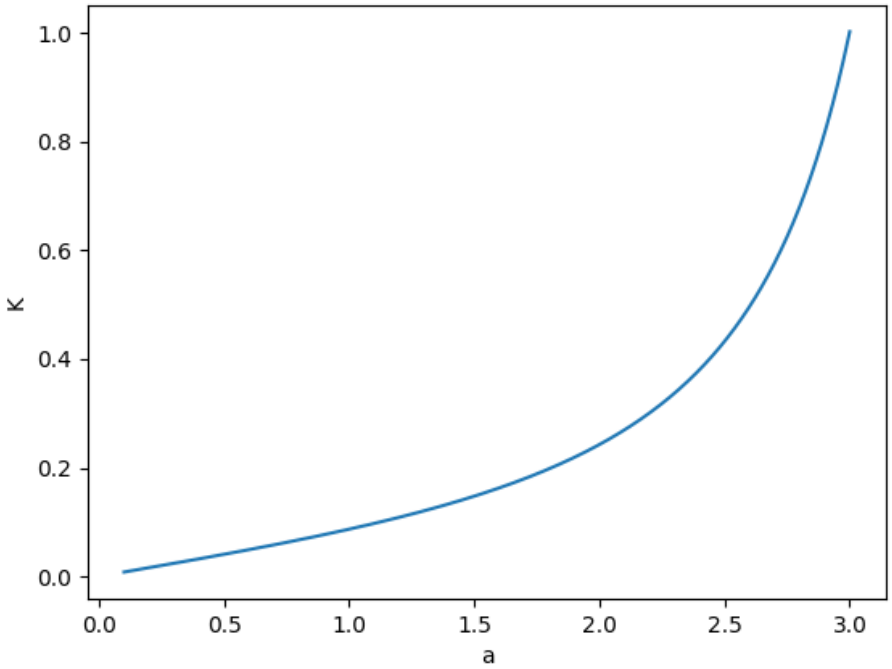

Figure 5.1: Single layer helicity dependence on α (Browning [2003]).

Next, the two layer model was built and surface plot was made with helicity plotted against α_1 and α_2 (Figure 5.2). When setting $\alpha_1 = \alpha_2$ then Figure 5.2 reduced to Figure 5.1 a useful check.

Both plots (Figure 5.1, Figure 5.2) show that as α (loosely defined as the twist of the field)

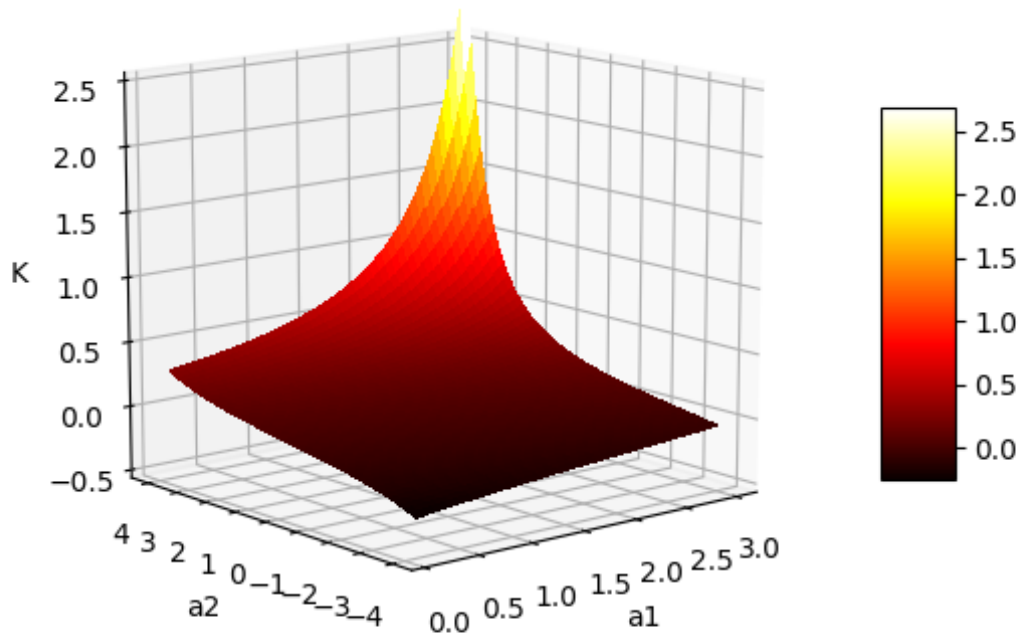

Figure 5.2: Surface plot of helicity for the two layer model, similar to Figure 7 in Browning [2003].

increased so too did the helicity (linkage and self linkage between the fields) as expected. After two layers however, it becomes more difficult to graphically display results to verify higher order models. Therefore we take a simpler approach moving forward, where we reduce the dimension of a higher order model to a lower order one. E.g computing the helicity when $\alpha_2 = \alpha_3$ in the three layer model it is possible to return the same helicity value using the two layer model.

Upon completion of the three layer code and reducing the dimension, it was seen that the same helicity plot could be obtained as the two layer code (Figure 5.2). Beyond that individual values were checked with the two layer model while varying the distance between layers in our model. After building the general multi-layer code we choose four layers and checked that it could reduce to the same value of helicity for the three layer code (Figure 5.3, Table 5.1, Table 5.2). Another check is when $\alpha_1 = \alpha_2 = ...\alpha_n$ and $-3.8 < \alpha < 3.8$, that $\delta W = 0$ (Table 5.3). The reason for limiting the range of α to $-3.8 < \alpha < 3.8$ is that the normalisation can tend to infinity close to these ranges (Figure 5.1, Figure 4.5) making the root finding algorithm unable

to obtain the relaxed α state. The last check was that $\delta W > 0$ for any α as only positive energy released is physical (Table 5.4).

In all we checked around 40 values by reducing the dimension, however only a few have been listed and can be seen in Table 5.1, Table 5.2, Table 5.3 and Table 5.4.

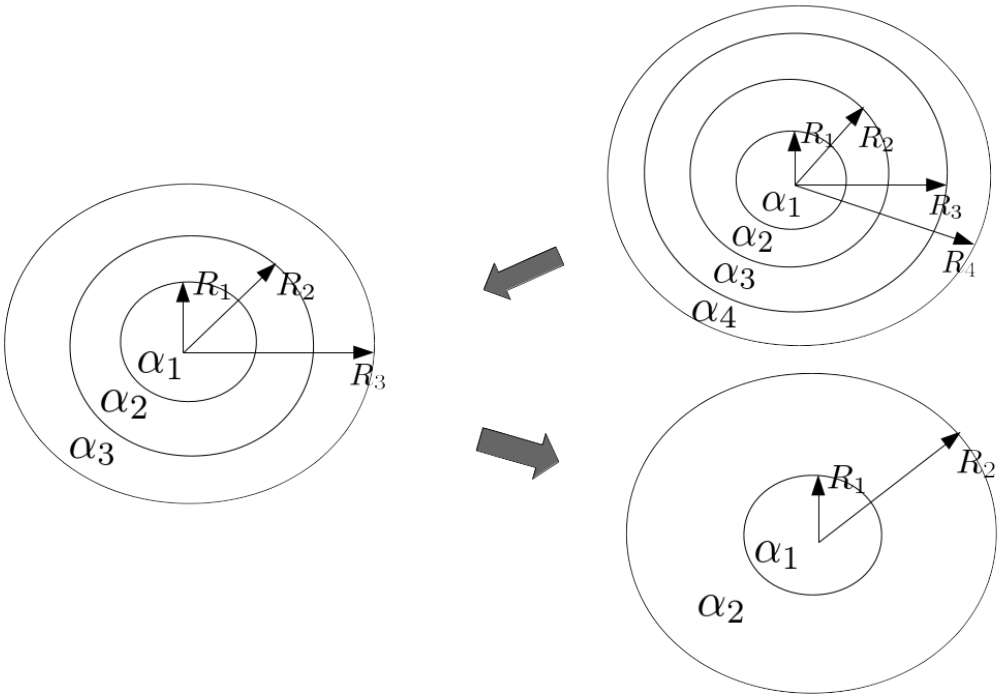

Figure 5.3: An aid to help visualise how the helicity for the a four layer model can be the same as in the three layer model when two adjacent layer have the same α value. The same applies going from a three to two layer model

R	α	**K**
0.25, 0.5, 0.75, 1	3, 3, -2, 4	0.111
0.25, 0.5, 0.75, 1	3, 3, 2, -3	0.225
0.25, 0.5, 0.75, 1	3, 2, 2, -3	-0.446

Table 5.1: Helicity values produced by the multi-layer code for comparison with three layer code (Table 5.2).

R	α	**K**
0.5, 0.75, 1	3, -2, 4	0.111
0.5, 0.75, 1	3, 2, -3	0.225
0.25, 0.75, 1	3, 2, -3	-0.446

Table 5.2: Helicity values produced by the three layer code for comparison with multi-layer code (Table 5.1).

R	α	δ**W**
0.2, 0.4, 0.6, 0.8, 1	2, 2, 2, 2, 2	-1×10^{-13}
0.25, 0.5, 0.75, 1	-3, -3, -3, -3	4×10^{-15}
0.25, 0.5, 0.75, 1	2.1, 2.1, 2.1, 2.1	5×10^{-15}

Table 5.3: Multi-layer code to show energy release for the same α values.

R	α	δ**W**
0.25, 0.5, 0.75, 1	2, 3, -5, 1	0.057
0.25, 0.5, 0.75, 1	2, -3, 6, 4	0.180
0.2, 0.4, 0.6, 0.8, 1	1, 3, 4, 2, -8	0.179

Table 5.4: Multi-layer code to show energy release values for a range of different α values.

5.2 Energy Release Results

A code to generate a linear α profile (Figure 5.4) was first generated, in order to verify how the gradient, γ of the linear α profile affected the energy released.

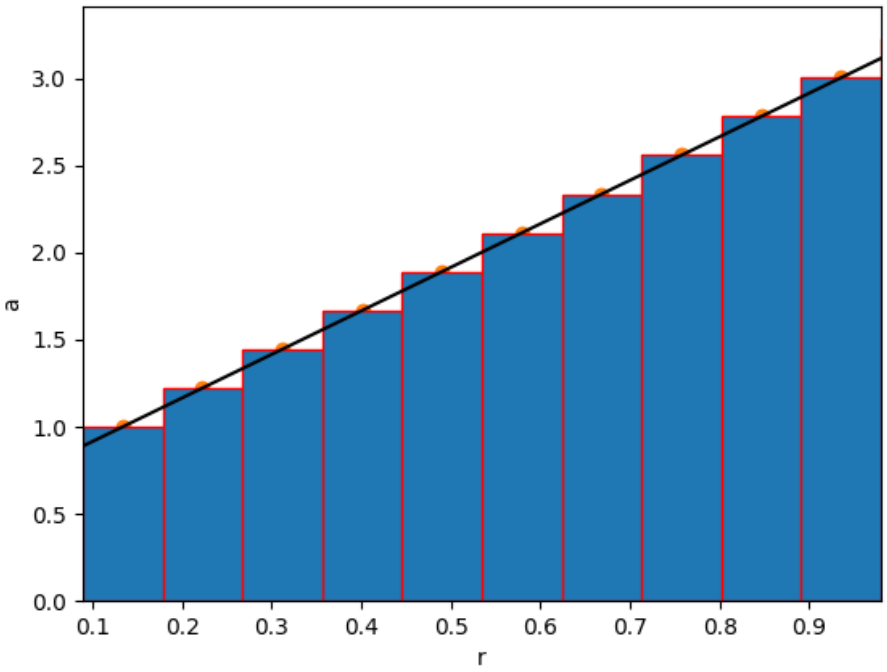

Figure 5.4: Approximate linear variation of α vs radius for 10 layers.

The gradient of the linear α profile was varied and after each variation a relaxation was carried out to obtain δW (Figure 5.5). Scaling the axis of Figure 5.5 by γ^2 shows a linear relationship between δW and γ (Figure 5.6). It can be seen that $\delta W \propto |\nabla\alpha|^2 \propto \gamma^2$ from (Van Ballegooijen and Cranmer [2008], Boozer [1986], Bhattacharjee and Hameiri [1986]) is obtained (Figure 5.6), increases the likelihood for hyperdiffusion as the mechanism for relaxation in our model.

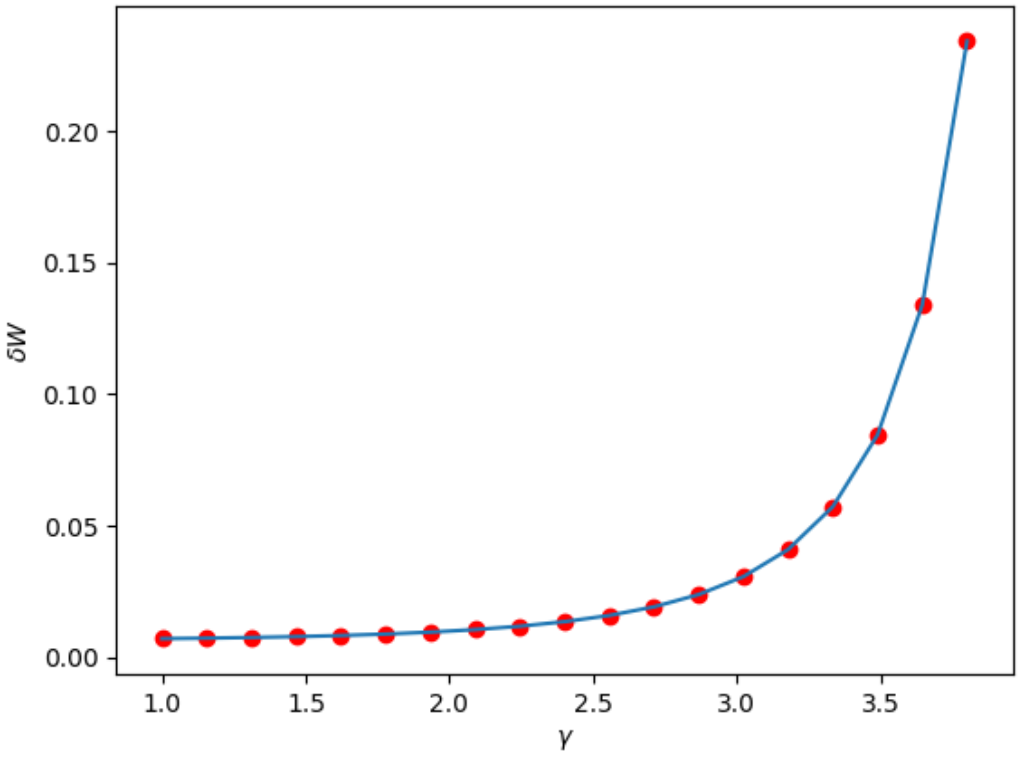

Figure 5.5: Relaxation of a 10 layer linear α profile Figure (5.4) each with increasing gradient, γ

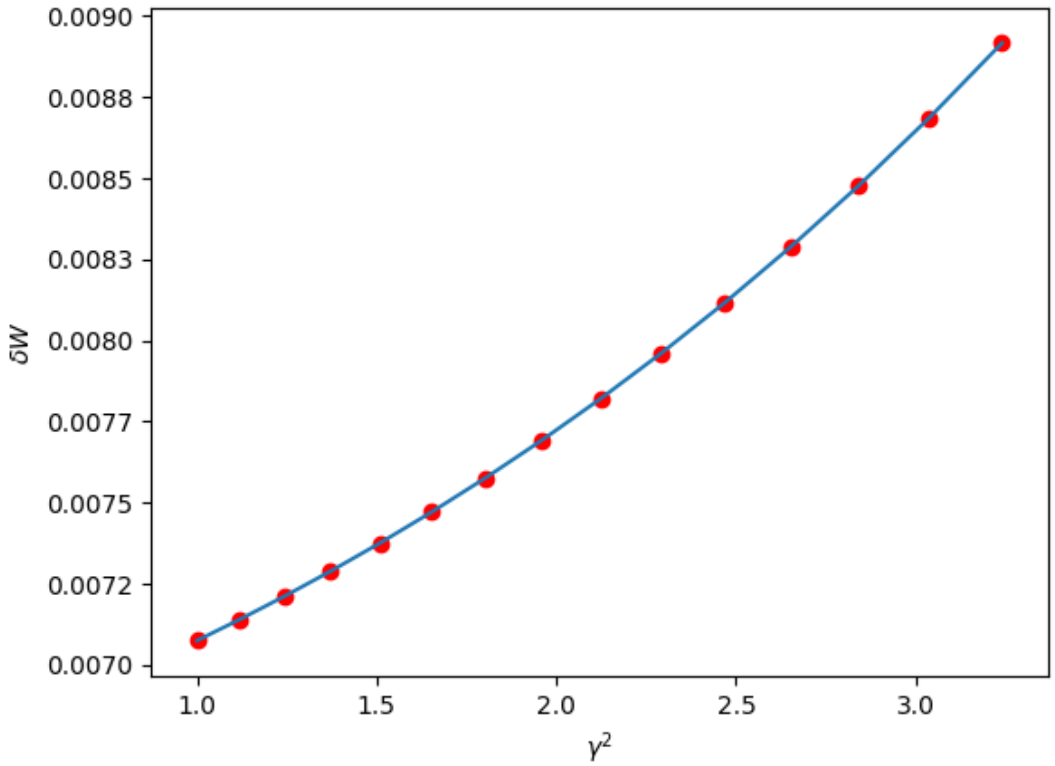

Figure 5.6: Relaxation of a 10 layer linear α profile Figure (5.4) each with increasing gradient squared, γ^2.

Initial α values were used from the linear profile (Figure 5.4) and gradient γ varied to observe the dependence on the change in helicity δK. The change in helicity was found by using the equation for helicity for any layer (4.16) with initial linear α values and subtracting (4.16) with the relaxed values for α. The transfer of helicity was then again calculated for increasing γ. The following figures can be compared by looking at the maximum value for the transfer of helicity δK between graphs of increasing γ. It was expected that the helicity would move from regions of low helicity to higher helicity, corresponding to small and large α values (Figure 5.1, Figure 5.4) and flattening out after relaxation. In practice mostly the opposite was obtained, that the helicity increased further in areas of already high α (Figure 5.7, Figure 5.8, Figure 5.9). The discrepancy may be a due to the large values of γ selected in the figures, as Figure 5.10 does show the helicity decreasing around regions of high α as expected. As expected plots showing the transfer of helicity (Figure 5.7, Figure 5.8, Figure 5.9, Figure 5.10) show $\delta K = 0$, when summing δK over r and are in line with helicity conservation. Finally the relationship $\delta K \propto |\nabla \alpha| \propto \gamma$ is not obtained (Van Ballegooijen and Cranmer [2008], Boozer [1986], Bhattacharjee and Hameiri [1986], Figure 5.7, Figure 5.8, Figure 5.9, Figure 5.10). Again the unexpected result seems likely due to the large step size of γ, such that the relaxed value for α is not at the true minimum energy state, hence the relationship between δK and γ may be skewed.

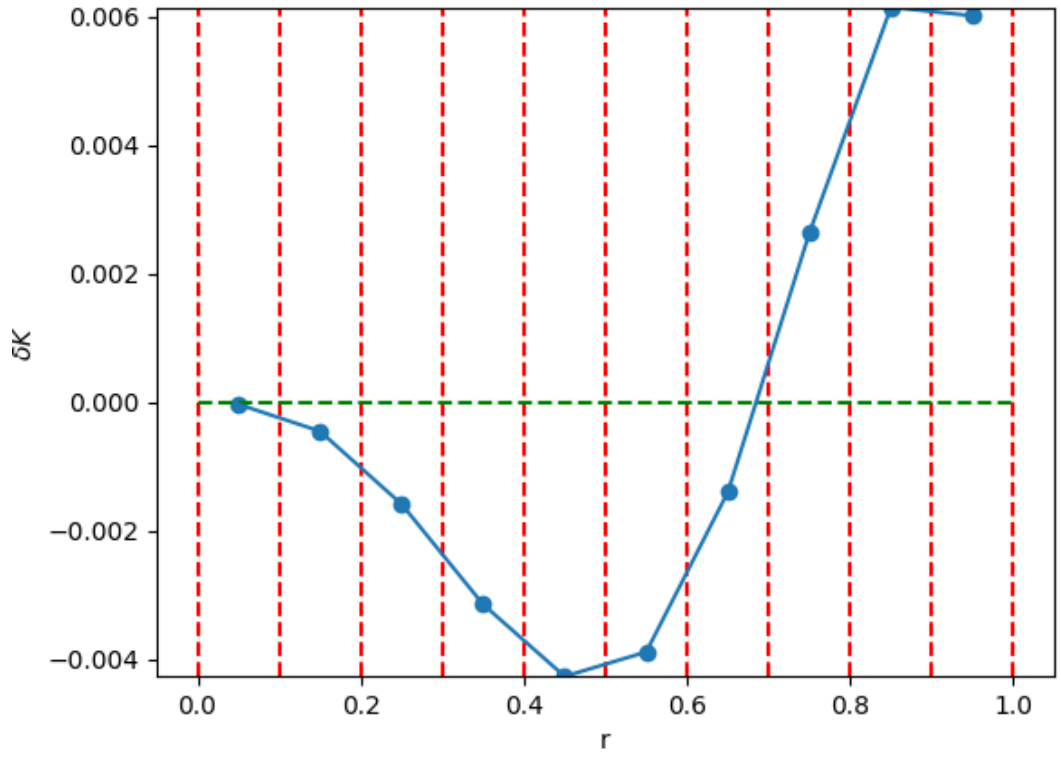

Figure 5.7: Change in helicity δK, within each layer for a 10 layer relaxation model for a linear α profile (Figure 5.4), $\gamma = 5$.

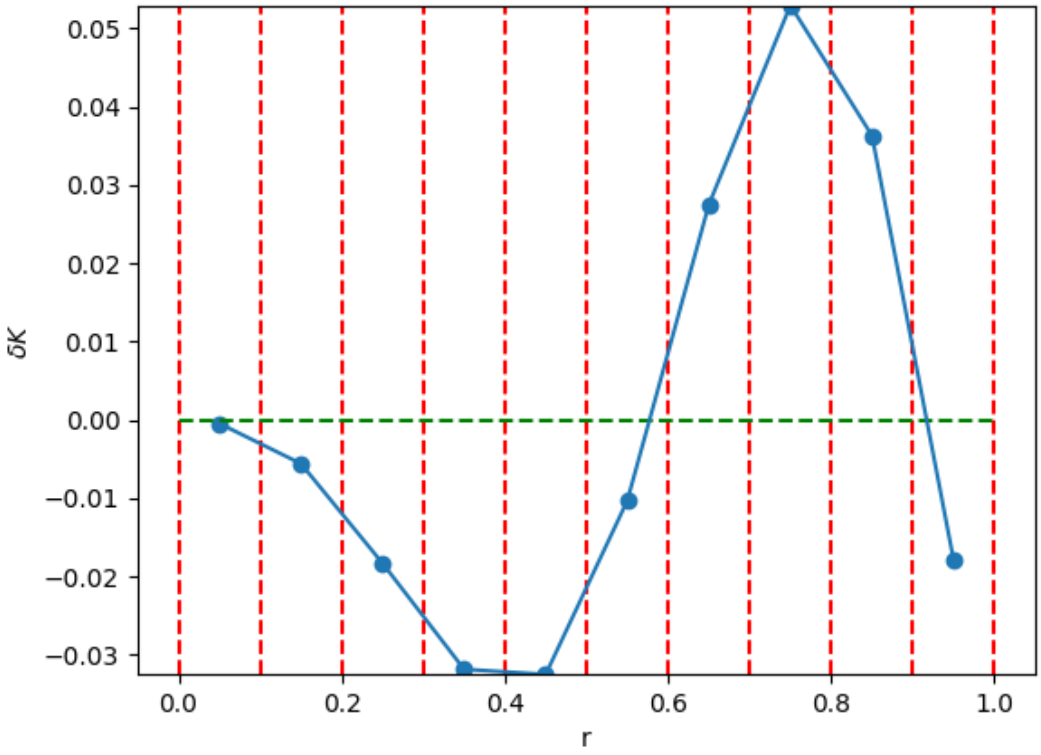

Figure 5.8: Change in helicity δK, within each layer for a 10 layer relaxation model for a linear α profile (Figure 5.4), $\gamma = 10$.

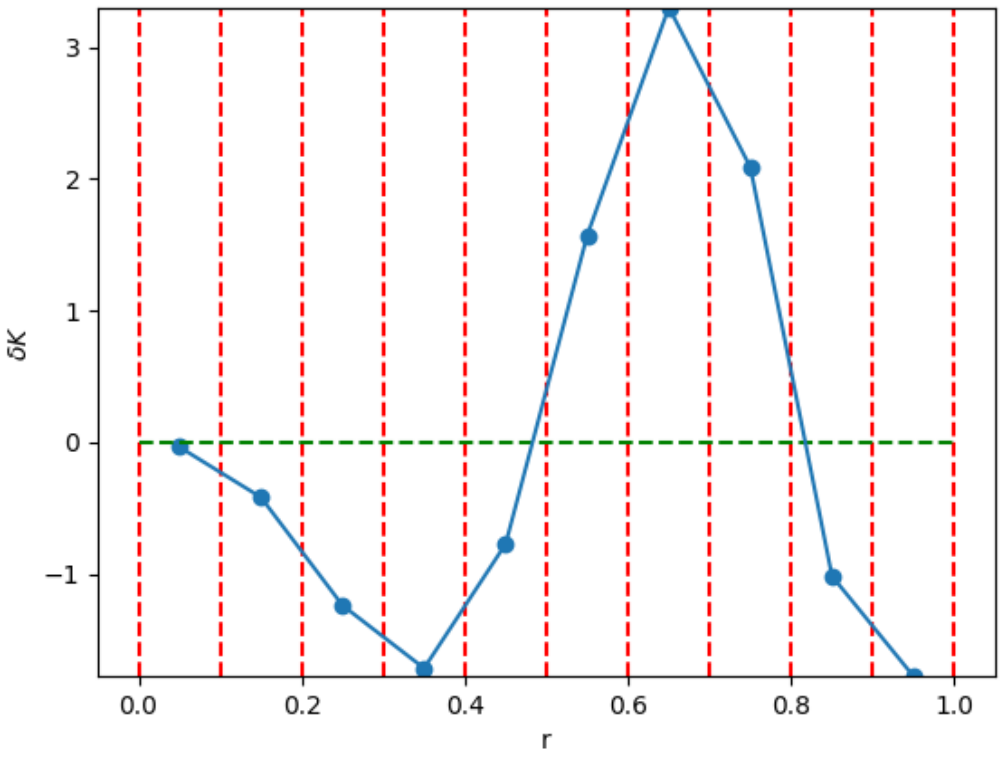

Figure 5.9: Change in helicity δK, within each layer for a 10 layer relaxation model for a linear α profile (Figure 5.4), $\gamma = 15$.

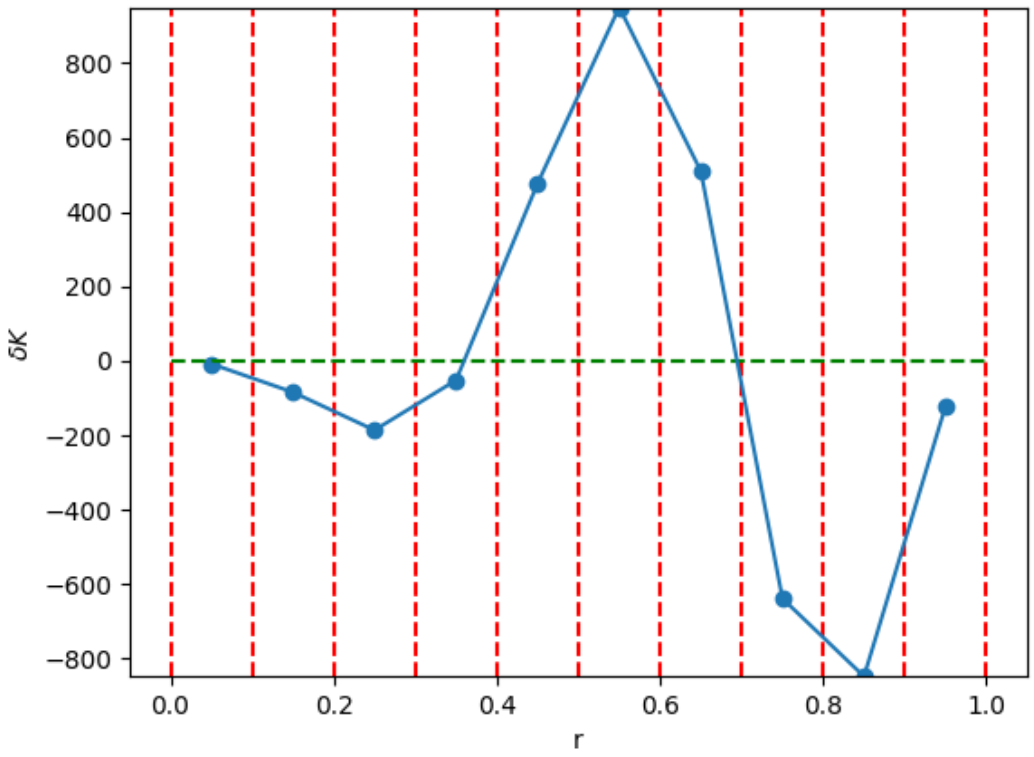

Figure 5.10: Change in helicity δK, within each layer for a 10 layer relaxation model for a linear α profile (Figure 5.4), $\gamma = 20$.

Now we look into the advantages of using the multi-layer code to solve otherwise numerical models. Rather than using resistive MHD simulations, it is possible to calculate helicity and energy for non analytic α profiles using our model such as for equations (4.9), (4.10), and (4.11), first used in Hood et al. [2009]. As the number of layers becomes large it becomes possible to generate almost continuous α profiles and obtain very accurate energy and helicity values. Now we now look into how the number of layers affects the accuracy for helicity ,energy and released energy values calculated from the field profiles (Figure 4.4, Figure 5.4). Finally the accuracy will be compared for both field profiles of a given number of layers.

Using the non-linear α profile (equation (4.11)), the discrepancy between helicity for 3 and 20 layers for can be seen to be almost a factor of 10 (Figure 5.12). Again for the non linear α profile, the energy difference between 3 and 20 layers was unexpectedly small (Figure 5.11), however this is not the energy released, δW. The value for δW would be much more skewed as it relies on α obtained from helicity conservation. It can be seen from Figure 5.13 which appears almost linear up to around 20 layers this could be due to the the discrepancy between both the energy Figure 5.11 and Figure 5.22.

For the linear α profile the difference between the helicity for 3 and 20 layers was equivalent to going from 1 to 3 layers (Figure 5.14). A similar difference was found for the energy, W for the same linear α profile (Figure 5.15). Taking the last figure for energy released Figure 5.16, all relations for the linear α profile (Figure 5.14, Figure 5.15, Figure 5.15) converge and look very similar as expected, another check for our model.

It was found that for a low number of layers the linear α (Figure 5.4) profile was closer to the convergent value than the non linear profile, as expected. Also for the non-linear profile δW was out by close to a factor of 10 (from 3 to 20 layers), this could be important when studying coronal heating using more realistic field profiles. A final point is that all calculations done in this paper with the multi-layer code have been fast, taking no longer than 5 seconds. Increasing the usefulness of the code to a large number of relaxation on an ensemble of coronal loops for example.

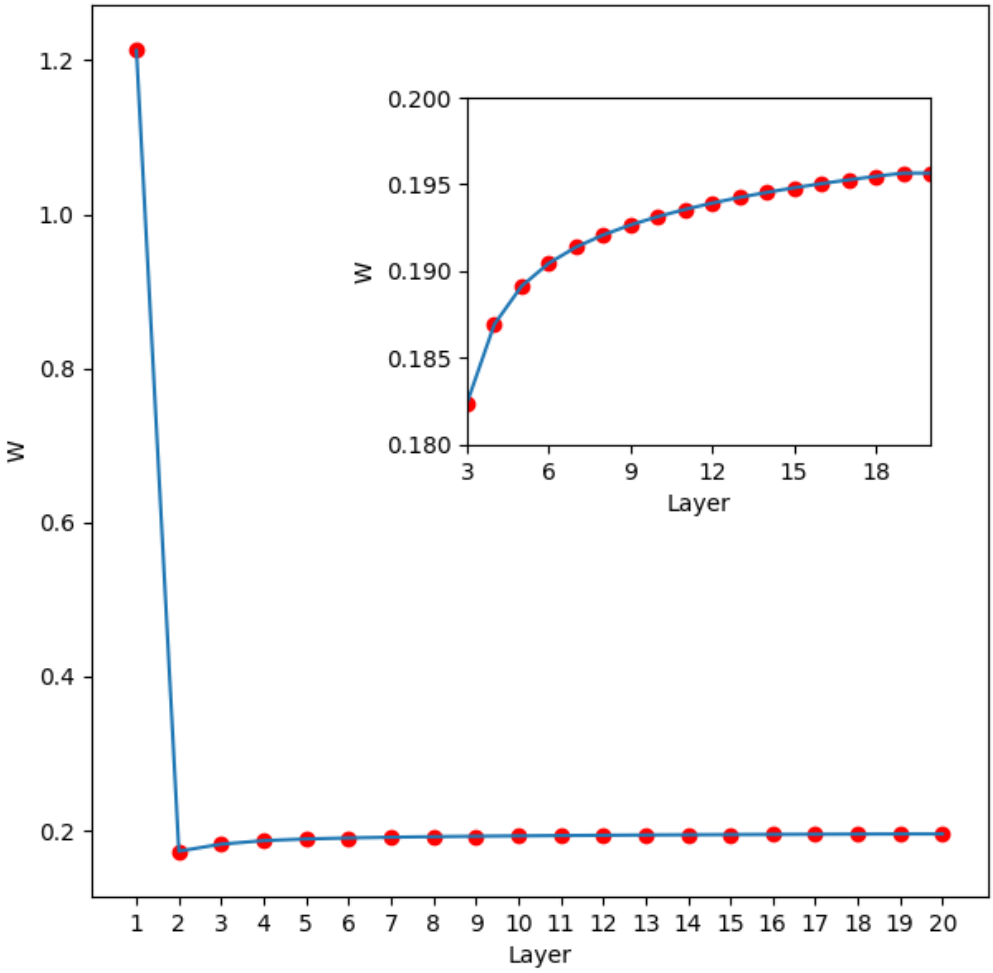

Figure 5.11: The dependence of intial energy on the number of layers, using the multi-layer model for the Hood et al. [2009] α profile, given in Figure 4.2.

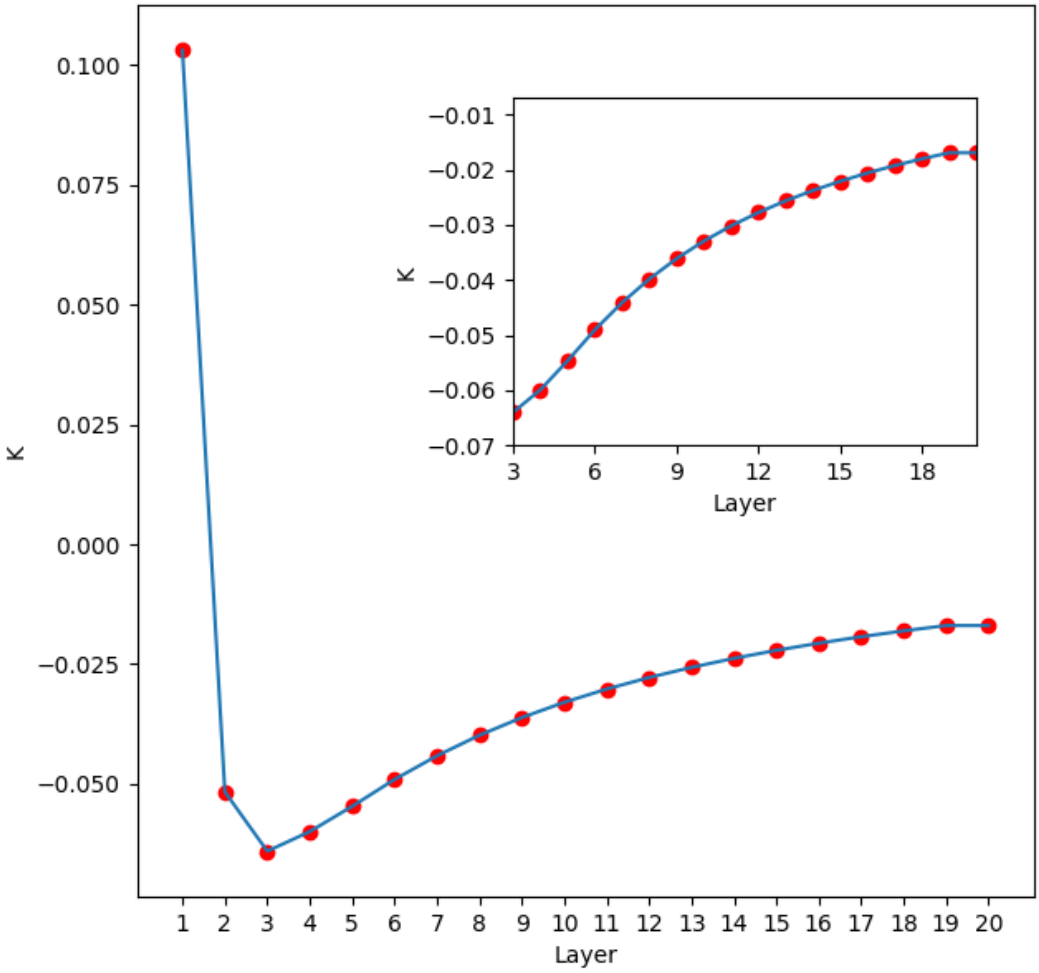

Figure 5.12: The dependence of initial helicity on the number of layers, using the multi-layer model for the Hood et al. [2009] α profile, given in Figure 4.2.

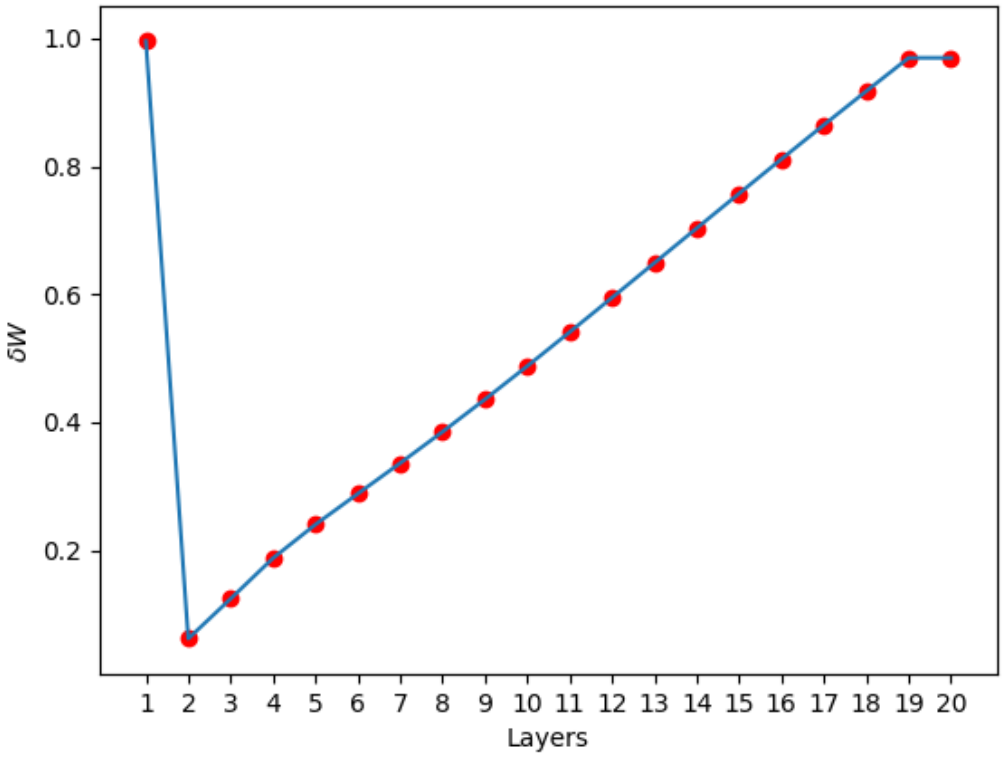

Figure 5.13: The dependence of energy released (relaxation) on the number of layers, using the multi-layer model, for the Hood et al. [2009] α profile, given in Figure 4.2.

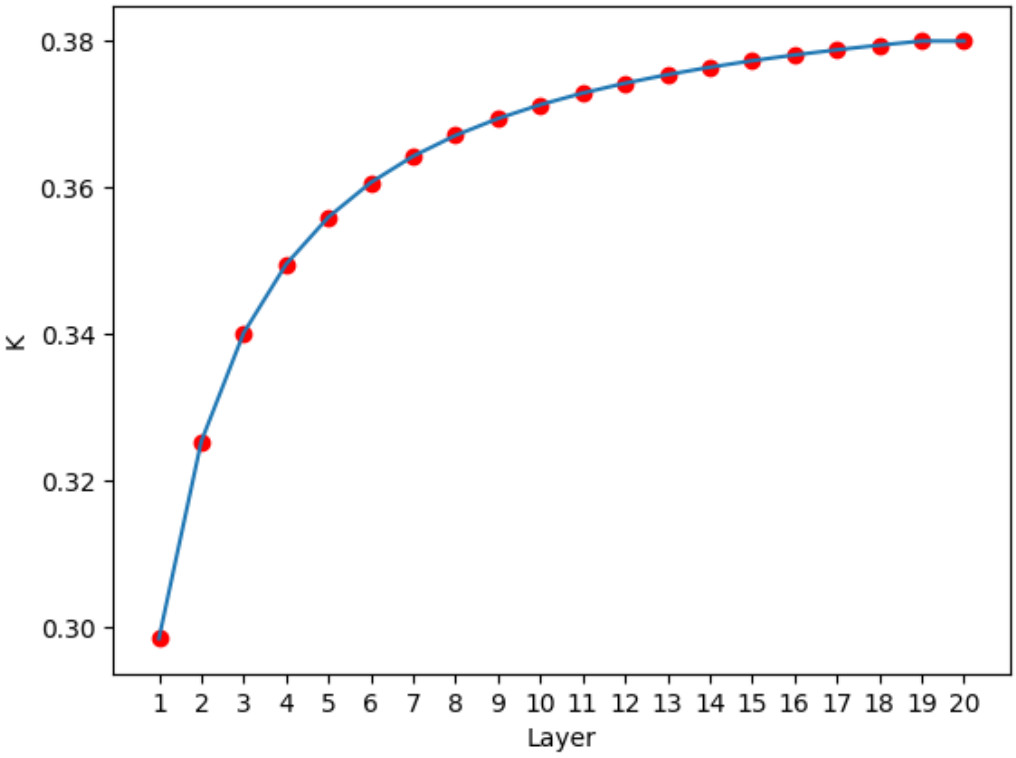

Figure 5.14: Dependence of intial helicity on the number of layers using the multi-layer model for the linear α profile, given in Figure 5.4.

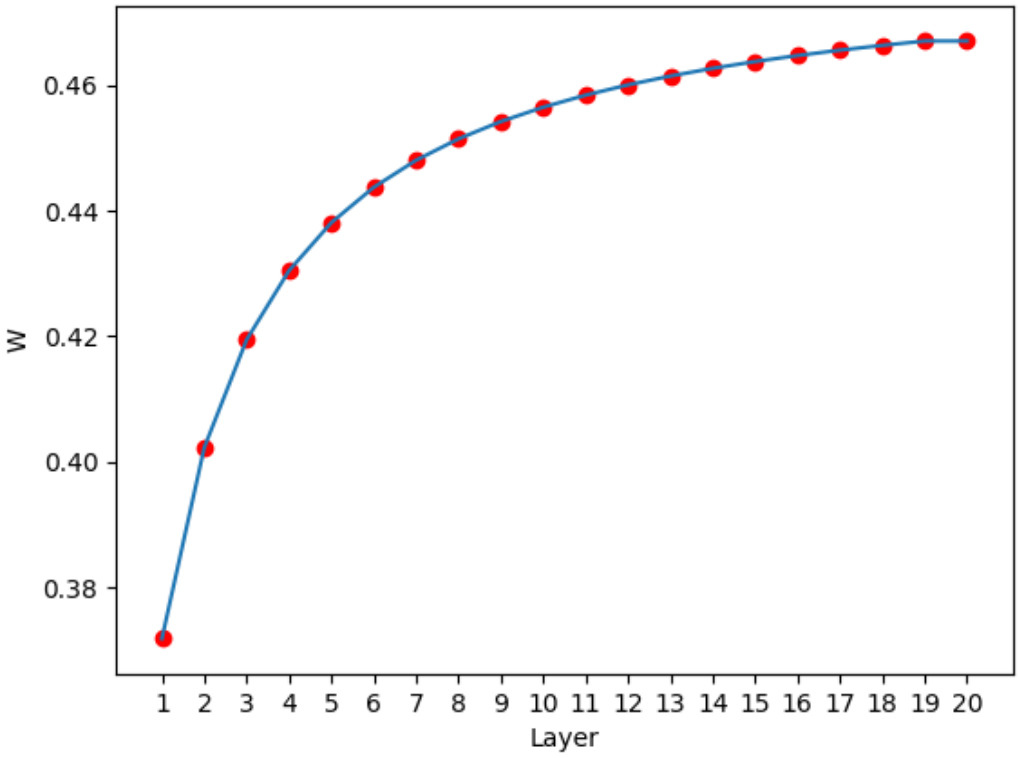

Figure 5.15: Dependence of intial energy on the number of layers using the multi-layer model for the linear α profile, given in Figure 5.4.

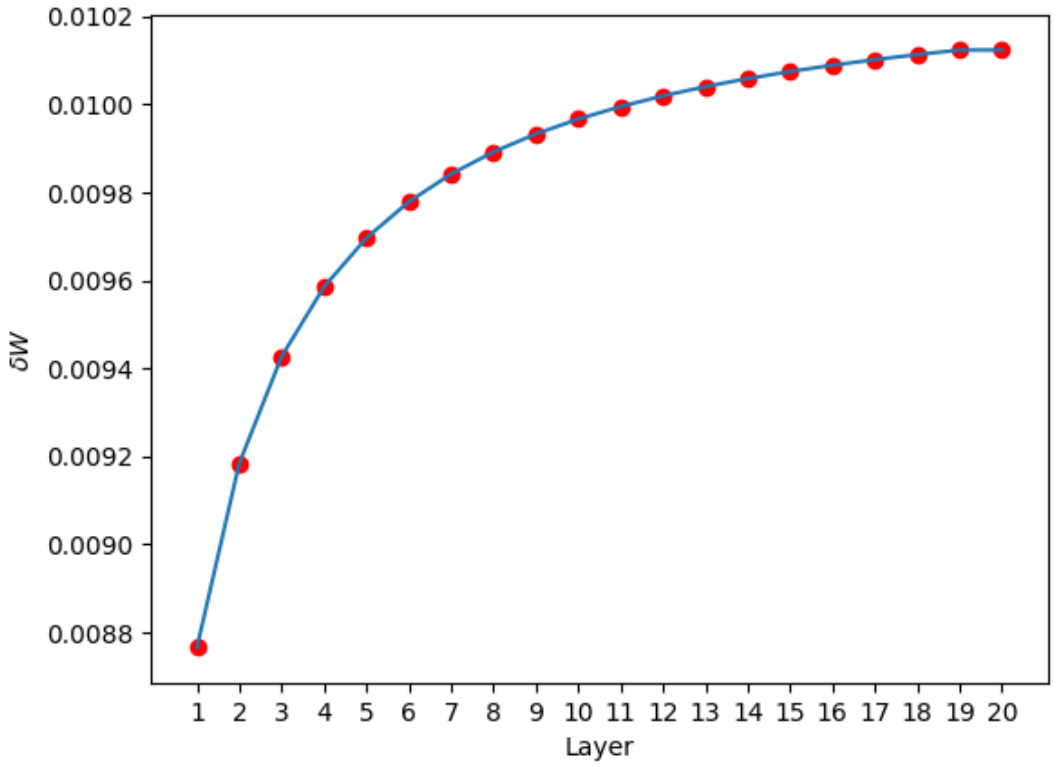

Figure 5.16: Dependence of energy released (relaxation) on the number of layers using the multi-layer model for the linear α profile, given in Figure 5.4.

Chapter 6

Discussion and Suggestions for further work

Cylindrical relaxation models have already been used to show DC heating is a viable mechanism to sustain coronal temperature (Browning [2003],Bareford et al. [2011]). In this thesis we further develop previous work on relaxation models (up to three layers) to any number of arbitrary layers. The model consists of concentric cylindrical tubes, with piece-wise constant functions of α, with B_z and B_θ that are continuous throughout.

I developed a multi-layer cylindrical relaxation code used to help verify the mechanism by which relaxation occurs. Using the code we set out to show if a turbulent MHD process known as hyperdiffusion (Van Ballegooijen and Cranmer [2008], Boozer [1986], Bhattacharjee and Hameiri [1986]) that diffuses the field while preserving the helicity, can predict relaxed values of energy and helicity transport in our model.

The multi-layer code calculated magnetic fields in a multi-layer cylindrical model, in which α is a constant in each layer: thus, the α profile has a 'stepped' form. Then the magnetic energy and helicity of the model is calculated. Finally, using the idea of Taylor's relaxation (Taylor [1974]) the energy release δW as the field relaxes to a constant-α field, conserving helicity, is calculated.

In developing the multi-layer code a large number of checks had to be performed in order to determine the validity of results. The main check used was dimensional reduction, where for

example, a three layer model should give the same helicity as a two layer model with two identical layers. Initially a single layer helicity profile was created, which was then compared with the helicity profile of a two layer model. Next, the three layer model was built and its helicity was compared to that of the two layer model. Eventually, a multi-layer model was created and compared with previous lower order models. The process of building higher order models, checking with lower order models and slowly moving forward allowed for a more robust code. Other checks for the the multi-layer code include that $\delta W > 0$ for any α. The last check for the multi-layer code was that $\delta W = 0$ for $\alpha_1 = \alpha_2 = \alpha_3 = ...\alpha_n$ and $-3.8 < \alpha < 3.8$ as only a certain range of α returns the true minimum energy state.

Two particular example profiles for $\alpha(r)$ were considered: a profile in which α depends linearly on r, and a profile with zero net current (used in Hood et al. [2009], Hussain et al. [2017]). Using the multi-layer code, the linear α profile was relaxed with varying gradient, γ to obtain the relationship $\delta W \propto |\nabla\alpha|^2 \propto \gamma^2$, in accordance with hyperdiffusion. Next we looked to probe the transfer of helicity to further confirm our hypothesis. To obtain the transfer of helicity we used an initial linear α profile with equation (4.16) (helicity for each layer), then we obtain α for the relaxed state and use it in (4.16) and subtracted the final helicity from the initial helicity of each layer to obtain δK vs r. However, considering the dependence of localised helicity changes, δK on γ, the expected relationship for hyperdiffusion $\delta K \propto |\nabla\alpha| \propto \gamma$ was not obtained. The unexpected result is most likely due to the values of γ used. Further analysis is needed to determine the correct relationship between δK and γ.

The multi-layer code is available on GitHub (github.com/shahbaz22/Solar). From the analysis it seems that more research is needed to explore the role of hyperdiffusion as the mechanism for cylindrical relaxation models and coronal heating. However, the work done in this thesis does give support to hyperdiffusion as a viable relaxation mechanism.

Multi-layer cylindrical models allow us better approximate field profiles, resulting in more accurate values of helicity and energy. The model is particularly useful for calculating helicity in fields where the exact integrals cannot be done analytically e.g. Hussain et al. [2017]. Therefore further extensions of this work could include comparing the multi-layer relaxation model to numerical resistive MHD simulations to determine its accuracy. It was also found that δW was out by around a factor of 10 (Figure 5.13), between 3 and 20 layers. Given the

speed of the multi-layer code, relaxations could be performed on an ensamble of loops using zero net current field profiles, building upon work in Bareford et al. [2011] and Hood et al. [2016]. Therefore a more accurate value for coronal heating via cylindrical relaxation models could be obtained. The accuracy of values obtained with the multi-layer code could help study magnetic reconnection as precise values are often needed on small scales.

Bibliography

J Allen, H Sauer, L Frank, and P Reiff. Effects of the march 1989 solar activity. *Eos, Transactions American Geophysical Union*, 70(46):1479–1488, 1989. doi: 10.1029/89EO00409.

T Amari and JF Luciani. Helicity Redistribution during Relaxation of Astrophysical Plasmas. Phys.Rev.Lett, 84(6):1196–1199, Feb 2000. doi: 10.1103/PhysRevLett.84.1196.

MR Bareford, PK Browning, and RAM Van der Linden. A nanoflare distribution generated by repeated relaxations triggered by kink instability. *Astronomy & Astrophysics*, 521:A70, 2010.

MR Bareford, PK Browning, and RAM Van der Linden. The flare-energy distributions generated by kink-unstable ensembles of zero-net-current coronal loops. *Solar Physics*, 273(1): 93–115, 2011.

MA Berger. Introduction to magnetic helicity. *Plasma Physics and Controlled Fusion*, 41(12B): B167, 1999.

MA Berger and GB Field. The topological properties of magnetic helicity. *Journal of Fluid Mechanics*, 147:133–148, 1984.

A Bhattacharjee and E Hameiri. Self-consistent dynamolike activity in turbulent plasmas. *Physical review letters*, 57(2):206, 1986.

Allen H Boozer. Ohm's law for mean magnetic fields. *Journal of plasma physics*, 35(1):133–139, 1986.

PK Browning, C Gerrard, AW Hood, R Kevis, and RAM Van der Linden. Heating the corona by nanoflares: simulations of energy release triggered by a kink instability. *Astronomy & Astrophysics*, 485(3):837–848, 2008.

Van der Linden RAM Browning, PK. Solar coronal heating by relaxation events. *Astronomy & Astrophysics*, 400(1):355–367, 2003.

TG Cowling. Magnetohydrodynamics. *Bristol, Adam Hilger, Ltd., 1976. 145 p.*, 1976.

AG Emslie, BR Dennis, GD Holman, and HS Hudson. Refinements to flare energy estimates: A followup to energy partition in two solar flare/cme events by ag emslie et al. *Journal of Geophysical Research: Space Physics*, 110(A11), 2005.

R Erdélyi, A Kerekes, and N Mole. In r. erdélyi, jl ballester, b. fleck (sci. eds.) soho 13-waves, oscillations and small-scale transient events in the solar atmosphere: A joint view from soho and trace. *ESA-SP*, 547:75, 2004.

MA Berger et al. On the dynamics of small-scale solar magnetic elements.

EW Weisstein. Bessel function of the first kind, from mathworld–a wolfram web resource. URL `http://mathworld.wolfram.com/BesselFunctionoftheFirstKind.html`. [Online; accessed 3rd December 2018].

J Finn and J Antonsen. Magnetic helicity: What is it and what is it good for? *Comments Plasma Phys. Controlled Fusion*, 9:111, 12 1984.

T Gold. *Magnetic Energy Shedding in the Solar Atmosphere*, volume 50, page 389. 1964.

L Golub and JM Pasachoff. *The solar corona*. Cambridge University Press, 2010.

W Gonzalez and E Parker. Magnetic reconnection. *Astrophysics and Space Science Library*, 427:10–1007, 2016.

J Heyvaerts and ER Priest. Coronal heating by reconnection in dc current systems-a theory based on taylor's hypothesis. *Astronomy and astrophysics*, 137:63–78, 1984.

J Heyvaerts and ER Priest. A self-consistent turbulent model for solar coronal heating. *The Astrophysical Journal*, 390:297–308, 1992.

JV Hollweg. Alfvén waves in the solar atmosphere. *Solar Physics*, 70(1):25–66, 1981.

GD Holman. Solar eruptive events. 2012.

AW Hood, PK Browning, and RAM Van der Linden. Coronal heating by magnetic reconnection in loops with zero net current. *Astronomy & Astrophysics*, 506(2):913–925, 2009.

AW Hood, PJ Cargill, PK Browning, and KV Tam. An mhd avalanche in a multi-threaded coronal loop. *The Astrophysical Journal*, 817(1):5, 2016.

AS Hussain, PK Browning, and AW Hood. A relaxation model of coronal heating in multiple interacting flux ropes. *Astronomy & Astrophysics*, 600:A5, 2017.

JAXA/Hinode, (June, 2013). URL `https://www.nasa.gov/centers/ames/news/2013/M13-40-iris-media-briefing.html`.

G Ji, Hand Huang and H Wang. The relaxation of sheared magnetic fields: a contracting process. *The Astrophysical Journal*, 660(1):893, 2007.

JA Klimchuk. Key aspects of coronal heating. *Phil. Trans. R. Soc. A*, 373(2042):20140256, 2015.

Lang, KR. Coronal heating graph, 2019. URL `http://ase.tufts.edu/cosmos/pictures/CambEncySunjpg`.

RM Lothian and PK Browning. Energy dissipation and helicity in coronal loops of variable cross-section. *Solar Physics*, 194(2):205–227, 2000.

D MacTaggart and A Hillier. Topics in magnetohydrodynamic topology, reconnection and stability theory. 2019.

DB Melrose, Jennifer Nicholls, and NG Broderick. Surface currents on models of force-free solar magnetic flux tubes. *Journal of plasma physics*, 51(1):163–176, 1994.

Dibyendu Nandy, Michael Hahn, Richard C. Canfield, and Dana W. Longcope. Detection of a taylor-like plasma relaxation process in the sun and its implication for coronal heating. *Proceedings of the International Astronomical Union*, 2004(IAUS223):473474, 2004. doi: 10.1017/S1743921304006568.

NASA/JPL-Caltech, (Sept, 2015). URL `https://photojournal.jpl.nasa.gov/catalog/PIA19822`.

NASA/SDO, Aug, 2012. URL `https://sdo.gsfc.nasa.gov/gallery/main/item/157`.

NASA/SDO, Dec, 2016. URL `https://sdo.gsfc.nasa.gov/gallery/main/item/765`.

Big Bear Solar Observatory, Aug, 2010. URL `https://www.eurekalert.org/pub`$_r eleases/2010-08/njio - san082410.php$.

EN Parker. Sweet's mechanism for merging magnetic fields in conducting fluids. *Journal of Geophysical Research*, 62(4):509–520, 1957.

EN Parker. Magnetic neutral sheets in evolving fields. i-general theory. *The Astrophysical Journal*, 264:635–647, 1983.

EN Parker. Nanoflares and the solar X-ray corona. ApJ, 330:474–479, July 1988. doi: 10.1086/166485.

HE Petschek. Magnetic field annihilation. *NASA Special Publication*, 50:425, 1964.

E Priest. Magnetic reconnection (magnetic reconnection, by eric priest and terry forbes, pp. 612. isbn 0521481791. cambridge, uk. *Cambridge University Press, June*, 2000:36, 2000.

ER Priest. *Solar magnetohydrodynamics*, volume 21. Springer Science & Business Media, 2012.

H Qin, W Liu, H Li, and J Squire. Woltjer-taylor state without taylors conjecture: Plasma relaxation at all wavelengths. *Physical review letters*, 109(23):235001, 2012.

E Robbrecht, D Berghmans, and RAM Van der Linden. Automated lasco cme catalog for solar cycle 23: are cmes scale invariant? *The Astrophysical Journal*, 691(2):1222, 2009.

DD Schnack. *Lectures in magnetohydrodynamics: with an appendix on extended MHD*, volume 780. Springer, 2009.

CJ Schrijver and KL Harvey. The photospheric magnetic flux budget. *Solar physics*, 150(1-2): 1–18, 1994.

A Steve and D Dennis. Solar eclipse, (July 11, 1991). Online; accessed 1st December 2018.

JB Taylor. Relaxation of Toroidal Plasma and Generation of Reverse Magnetic Fields. *Physical Review Letters*, 33:1139–1141, November 1974. doi: 10.1103/PhysRevLett.33.1139.

JB Taylor. Relaxation and magnetic reconnection in plasmas. *Reviews of Modern Physics*, 58: 741–763, July 1986. doi: 10.1103/RevModPhys.58.741.

NASA TRACE, (Nov, 2000). URL `http://www.lmsal.com/TRACE/POD/images/arcade`$_{9n}ov_2000.gif$.

AA Van Ballegooijen and SR Cranmer. Hyperdiffusion as a mechanism for solar coronal heating. *The Astrophysical Journal*, 682(1):644, 2008.

GE Vekstein, ER Priest, and CDC Steele. Magnetic reconnection and energy release in the solar corona by taylor relaxation. *Solar Physics*, 131(2):297–318, 1991.

AL Wilmot-Smith, DI Pontin, AR Yeates, and G Hornig. Heating of braided coronal loops. *Astronomy & Astrophysics*, 536:A67, 2011.

L Woltjer. On the theory of hydromagnetic equilibrium. *Reviews of Modern Physics*, 32(4): 914, 1960.

AR Yeates, G Hornig, and AL Wilmot-Smith. Topological constraints on magnetic relaxation. *Phys. Rev. Lett.*, 105:085002, Aug 2010. doi: 10.1103/PhysRevLett.105.085002.